



AFRL-AFOSR-VA-TR-2016-0302

Heterogeneously Catalyzed Endothermic Fuel Cracking

**Anthony Dean
COLORADO SCHOOL OF MINES
1500 ILLINOIS ST
GOLDEN, CO 80401-1887**

**08/28/2016
Final Report**

DISTRIBUTION A: Distribution approved for public release.

Air Force Research Laboratory
AF Office Of Scientific Research (AFOSR)/RTB2

REPORT DOCUMENTATION PAGE				Form Approved OMB No. 0704-0188	
<p>The public reporting burden for this collection of information is estimated to average 1 hour per response, including the time for reviewing instructions, searching existing data sources, gathering and maintaining the data needed, and completing and reviewing the collection of information. Send comments regarding this burden estimate or any other aspect of this collection of information, including suggestions for reducing the burden, to the Department of Defense, Executive Service Directorate (0704-0188). Respondents should be aware that notwithstanding any other provision of law, no person shall be subject to any penalty for failing to comply with a collection of information if it does not display a currently valid OMB control number.</p> <p>PLEASE DO NOT RETURN YOUR FORM TO THE ABOVE ORGANIZATION.</p>					
1. REPORT DATE (DD-MM-YYYY) 27-07-2016		2. REPORT TYPE Final		3. DATES COVERED (From - To) 30-09-2012 to 31-05-2016	
4. TITLE AND SUBTITLE Heterogeneously Catalyzed Endothermic Fuel Cracking				5a. CONTRACT NUMBER	
				5b. GRANT NUMBER FA9550-12-1-0495	
				5c. PROGRAM ELEMENT NUMBER	
6. AUTHOR(S) C. Karakaya, S. DeCaluwe, R. J. Kee, M. Saldana, G. Bogin, Jr., A. M. Dean (Colorado School of Mines) S. Opalka, T. Zheu, H. Huang (United Technologies Research Center) R. Lobo, D. G. Vlachos, E. Schreiner, T. Forsido, H. Shen (Univ. Delaware)				5d. PROJECT NUMBER	
				5e. TASK NUMBER	
				5f. WORK UNIT NUMBER	
7. PERFORMING ORGANIZATION NAME(S) AND ADDRESS(ES) Trustees of the Colorado School of Mines 1500 Illinois Street Golden, CO 80401				8. PERFORMING ORGANIZATION REPORT NUMBER	
9. SPONSORING/MONITORING AGENCY NAME(S) AND ADDRESS(ES) AF Office of Scientific Research 875 North Randolph Street, Rm. 3112 Arlington, VA 22203				10. SPONSOR/MONITOR'S ACRONYM(S) USAF, AFRL	
				11. SPONSOR/MONITOR'S REPORT NUMBER(S)	
12. DISTRIBUTION/AVAILABILITY STATEMENT DISTRIBUTION A: Distribution approved for public release.					
13. SUPPLEMENTARY NOTES					
14. ABSTRACT The objective of this project was to develop and apply fundamentally based experimental and computational methodologies that can lead to the design of improved supercritical fuel/catalyst/heat exchanger systems for cooling hypersonic vehicles. This project was a multi-team effort involving researchers at the University of Delaware, United Technologies Research Center, and the Colorado School of Mines. Models were developed to describe high-pressure chemically reacting processes, including those operating in the supercritical regime. Multiple catalysis were experimentally characterized and used to characterize hydrocarbon cracking reactions. Density functional calculations were applied to characterize the impact of varying the Si/Al ratio in certain zeolites. Comparisons of conversion, major product distributions and molecular weight growth processes in the gas-phase pyrolysis of model fuels to a detailed kinetic mechanism demonstrated that the mechanism could properly describe the impact of wide variations in pressure, including supercritical pressures. Candidate catalysts were successfully tested under supercritical fuel conditions in the UTRC heat exchanger rig.					
15. SUBJECT TERMS Endothermic fuels, supercritical conditions, catalysts, kinetic models, catalyst characterization, heat exchanger tests					
16. SECURITY CLASSIFICATION OF:			17. LIMITATION OF ABSTRACT	18. NUMBER OF PAGES	19a. NAME OF RESPONSIBLE PERSON
a. REPORT	b. ABSTRACT	c. THIS PAGE			Anthony M. Dean
U	U	U	N/A		19b. TELEPHONE NUMBER (Include area code) 303-273-3643

INSTRUCTIONS FOR COMPLETING SF 298

1. REPORT DATE. Full publication date, including day, month, if available. Must cite at least the year and be Year 2000 compliant, e.g. 30-06-1998; xx-06-1998; xx-xx-1998.

2. REPORT TYPE. State the type of report, such as final, technical, interim, memorandum, master's thesis, progress, quarterly, research, special, group study, etc.

3. DATES COVERED. Indicate the time during which the work was performed and the report was written, e.g., Jun 1997 - Jun 1998; 1-10 Jun 1996; May - Nov 1998; Nov 1998.

4. TITLE. Enter title and subtitle with volume number and part number, if applicable. On classified documents, enter the title classification in parentheses.

5a. CONTRACT NUMBER. Enter all contract numbers as they appear in the report, e.g. F33615-86-C-5169.

5b. GRANT NUMBER. Enter all grant numbers as they appear in the report, e.g. AFOSR-82-1234.

5c. PROGRAM ELEMENT NUMBER. Enter all program element numbers as they appear in the report, e.g. 61101A.

5d. PROJECT NUMBER. Enter all project numbers as they appear in the report, e.g. 1F665702D1257; ILIR.

5e. TASK NUMBER. Enter all task numbers as they appear in the report, e.g. 05; RF0330201; T4112.

5f. WORK UNIT NUMBER. Enter all work unit numbers as they appear in the report, e.g. 001; AFAPL30480105.

6. AUTHOR(S). Enter name(s) of person(s) responsible for writing the report, performing the research, or credited with the content of the report. The form of entry is the last name, first name, middle initial, and additional qualifiers separated by commas, e.g. Smith, Richard, J, Jr.

7. PERFORMING ORGANIZATION NAME(S) AND ADDRESS(ES). Self-explanatory.

8. PERFORMING ORGANIZATION REPORT NUMBER. Enter all unique alphanumeric report numbers assigned by the performing organization, e.g. BRL-1234; AFWL-TR-85-4017-Vol-21-PT-2.

9. SPONSORING/MONITORING AGENCY NAME(S) AND ADDRESS(ES). Enter the name and address of the organization(s) financially responsible for and monitoring the work.

10. SPONSOR/MONITOR'S ACRONYM(S). Enter, if available, e.g. BRL, ARDEC, NADC.

11. SPONSOR/MONITOR'S REPORT NUMBER(S). Enter report number as assigned by the sponsoring/monitoring agency, if available, e.g. BRL-TR-829; -215.

12. DISTRIBUTION/AVAILABILITY STATEMENT. Use agency-mandated availability statements to indicate the public availability or distribution limitations of the report. If additional limitations/ restrictions or special markings are indicated, follow agency authorization procedures, e.g. RD/FRD, PROPIN, ITAR, etc. Include copyright information.

13. SUPPLEMENTARY NOTES. Enter information not included elsewhere such as: prepared in cooperation with; translation of; report supersedes; old edition number, etc.

14. ABSTRACT. A brief (approximately 200 words) factual summary of the most significant information.

15. SUBJECT TERMS. Key words or phrases identifying major concepts in the report.

16. SECURITY CLASSIFICATION. Enter security classification in accordance with security classification regulations, e.g. U, C, S, etc. If this form contains classified information, stamp classification level on the top and bottom of this page.

17. LIMITATION OF ABSTRACT. This block must be completed to assign a distribution limitation to the abstract. Enter UU (Unclassified Unlimited) or SAR (Same as Report). An entry in this block is necessary if the abstract is to be limited.

Heterogeneously Catalyzed Endothermic Fuel Cracking (FA9550-12-1-0495)

Final Report

July 27, 2016

Overview

The objective of this project was to develop and apply fundamentally based experimental and computational methodologies that can lead to the design of improved supercritical fuel/catalyst/heat exchanger systems for cooling hypersonic vehicles. The approach was to develop a molecular-level understanding of the coupled homogeneous and heterogeneous reacting fuel processes to: (a) increase heterogeneous catalyst selectivity for fuel endothermic cracking to ethylene and hydrogen, thereby maximizing the extent of cooling, (b) increase catalyst activity for fuel decomposition, but inhibit gas-phase molecular weight growth reactions leading to deposit formation, and (c) identify flow conditions that maximize heat transfer and fuel contact with the catalyst while minimizing the time required for the fuel to be in the hot zone, thereby inhibiting undesired gas-phase reactions. The complexities of this system required a multiscale model, grounded in theory, to identify the most promising regimes in which to focus the experimental effort. This project was a multi-team effort involving researchers at the University of Delaware [UDEL] (Dr. Raul F. Lobo and Dr. Dion G. Vlachos, PIs), United Technologies Research Center [UTRC] (Dr. Susanne M. Opalka and Dr. Meredith B. Colket, PIs), and the Colorado School of Mines [CSM] (Dr. Gregory E. Bogin, Jr., Dr. Robert J. Kee, and Dr. Anthony M. Dean, PIs). All three institutions engaged in experimental and computational efforts. The project team defined complementary roles and identified conditions for the reactor and computational studies at each site to facilitate benchmarking and communication of standardized results. This report summarizes the overall effort. CSM was granted a six month no-cost extension through May 31, 2016 to allow completion of pressure-dependent experiments and kinetic model development for the gas-phase pyrolysis of ethane and pentane. There will be a more extensive report on these efforts since the other results were discussed in more detail in our last annual report (October 2015).

Colorado School of Mines

Modeling Heterogeneous Catalysis for Endothermic Fuel Pyrolysis

Canan Karakaya, Steven DeCaluwe, and Robert J. Kee

Broadly speaking, the modeling research spans three synergistically related topics:

1. Developing and applying modeling and software tools to high-pressure chemically reacting processes, including supercritical behavior,
2. Developing models to evaluate the influence of low levels of steam addition for reducing the production of polyaromatics and mitigating catalyst-fouling carbon deposits,
3. Developing new microstructural models to represent catalytic performance in washcoated monolith structures.

High and supercritical pressure

To support applications such as hypersonic combustion, the endothermic fuel-pyrolysis reactors need to operate at pressure around 50 bar. At such high pressures, the gas-phase behaves as a “real gas” in the sense that equations of state, thermodynamic properties, transport properties, and reaction-rate expressions do not always comply with ideal-gas representations. Throughout this BRI project, we have extended the CANTERA software to accommodate such non-ideal behavior. The approach is based generally on a multicomponent Redlich-Kwong equation of state, with self-consistent thermodynamic and transport properties. The modeling tools have been applied to assist the interpretation of high-pressure flow-reactor measurements at the Colorado School of Mines and at the University of Delaware.

Oxygen and steam addition

Essentially all high-temperature catalytic pyrolysis processes must contend with the catalyst fouling and deactivation processes that are associated with polyaromatic hydrocarbons (PAH) and coke formation. Even with perfectly selective catalysts, gradual degradation of the catalyst is inevitable under non-oxidative conditions. Coke and higher polyaromatic hydrocarbons (PAH) are thermodynamically favored over the desired aliphatic and olefinic products. There is compelling evidence that low levels of steam (e.g., below 1 percent) can play a beneficial role in reducing molecular-weight growth and mitigating carbon deposits. The steam can remove graphitic carbon deposits via direct reaction as [1-3]



The PAH formation probabilities and rates increase with increasing fuel carbon number. That is, in a jet fuel mixture where the average carbon number is 9-16, it is more likely that the catalyst fouling and deactivation is via PAH formation mechanism.

The formation of PAH species begins with cyclization, forming benzene, toluene and xylene, followed by the molecular-weight growth initially forming naphthalene and its derivatives (e.g., methyl naphthalene). Naphthalene is a primary precursor for further PAH growth. Naphthalene reacts rapidly to form higher polyaromatics, (e.g., anthracene, phenanthrene, fluoranthene, pyrene,...), which can condense to form deleterious solid deposits on the catalyst. These species can block zeolite cage openings, inhibiting transport into and out of the small channels, or cover active catalyst sites and block reactant adsorption. In either case, the result appears as catalyst deactivation or loss of activity.

In non-oxidative reaction environments, if the naphthalene formation and the further cyclization reactions can be avoided, the catalyst deactivation can be controlled as well. Low levels of H₂O can react beneficially with naphthalene, interrupting the pathway to higher PAH. The reaction products (including hydrogen, carbon monoxide, ethylene,...) also beneficially affect the endothermic dehydrogenation process by producing combustion fuels with reduced ignition-delay times. Thus, as illustrated in Fig. 1, low-level steam addition can serve to increase the effective formation rates of H₂ and small olefins, and decrease PAH growth rates and deposit formation [4].

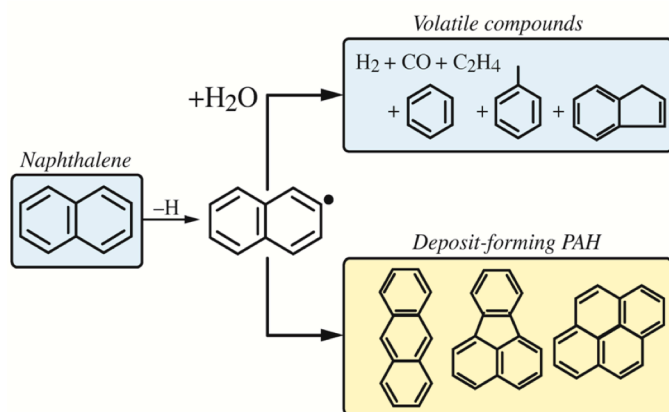


Fig 1: Schematic illustrating possible pathways for the interactions of steam with naphthalene

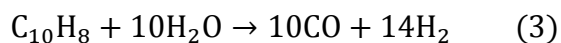
Buchireddy et al. [5] studied naphthalene steam cracking in a packed-bed reactor with a synthesis gas (20% CO, 9% CO₂, 20% H₂, 3% CH₄), C₁₀H₈ and H₂O at 750°C and a steam-to-carbon ratio of 5.0. They proposed that cracking reactions take place within the zeolite cage structure at Brønsted acid sites. Therefore, higher acidity tends to increase naphthalene cracking activity. Because naphthalene must be transported

inside the zeolite cages, the cage size strongly influences the cracking rate. Zeolites with larger cages tend to produce higher cracking activity. For example, H-ZSM-5, which has a characteristic cage dimension of 55 nm, delivers 19% naphthalene conversion. The ZY-30, which has a characteristic cage dimension of 80 nm, increased the naphthalene conversion to 33%.

Buchireddy et al. suggested that the naphthalene cracking produces graphitic carbon C(s) as well as volatile CO, CO₂ and smaller hydrocarbons. The surface carbon reacts further with H₂O (Eq.1) and CO₂ to form CO (Eq.2).



Incorporating Ni into zeolites can significantly increase the naphthalene conversion up to 98%. Buchireddy et al. explained the high conversion by the Ni promoting steam and dry reforming as [5]



Buchireddy et al. measured naphthalene conversion, but did not report the product composition. Thus, the chemical pathways of steam-naphthalene interaction remain unclear. Nevertheless, based on thermodynamics considerations, steam reforming of naphthalene should be fast above 700°C. The Gibbs free energy change of the naphthalene-steam-reforming reaction (Eq.3) is $\Delta G = -66 \text{ kJ mol}^{-1}$ at 750 °C.

Naphthalene steam cracking is certainly not limited to zeolite catalysts. Devi et al. [4] studied naphthalene steam cracking over olivine (Mg-Fe silicate) catalysts and proposed a detailed reaction pathway. The suggested pathway begins at naphthalene, with gas-phase products including benzene, toluene, ethylene, indene and acetylene. The reaction mechanism also includes PAH species including fluoranthene, anthracene, phenanthracene, crysene, and pyrene.

Wang et al. [6] proposed a reaction pathway for naphthalene steam cracking over Rh₂O₃/HY zeolite and Mo-Ni oxide catalysts. In this reaction pathway, naphthalene ring opening favors the formation of smaller smaller alkanes and aromatics. However hydrogenation reactions proceed in parallel with steam cracking, producing very large polyaromatic hydrocarbons (i.e., teralin and decalin) through condensation reactions.

In addition to dominantly catalytic chemistry, gas-phase reactions may also play important roles, especially at high temperature. Jess [7] studied homogeneous gas-phase reaction of naphthalene and steam at temperatures between 700 and 1400 °C. Although naphthalene is difficult to activate homogeneously at temperatures below 750°C, at higher temperatures numerous gas-phase products were measured (CO, CO₂, C₂H₂, C₂H₄, C₂H₆, C₆H₆ and C₇H₈, C₉H₈ and C₉H₁₀). These gas-phase species are also products of catalytic naphthalene steam cracking processes[4,6]. Although gas-phase chemistry may be active, the catalyst certainly affects reaction pathways and the product distribution.

It is important to note that the steam-naphthalene reactions may compete with the undesired reforming pathway. Fortunately, with very low steam levels, the desired endothermicity is only weakly affected.

Research this year has focused first on finding, studying, and assimilating the relevant literature on the effects of steam and oxygen addition in non-oxidative environments. Much of this literature is in the context of gas-to-liquids technology and industrial dehydrogenation processes. Based on the published measurements, we are developing global representations of the relevant reaction chemistry. The global steam reactions are integrated with the detailed methane dehydroaromatization (MDA) chemistry developed earlier in the project [8].

Future research could investigate the possibility of steam addition via ceramic oxygen-ion-conducting membranes. As an alternative to premixing steam with the parent fuel, some advantages can be gained by distributed steam introduction via membranes along the length of the reactor.

Catalyst washcoats

Most published studies on dehydrogenation processes and fuel pyrolysis are based upon catalysts in the packed-bed configuration. However, such catalyst packing leads to relatively high pressure drops that might be detrimental to overall systems performance. Washcoated monoliths or microchannel reactors offer potentially beneficial alternatives.

A major effort this year focused on developing and applying a focused-ion-beam--scanning-electron-microscope (FIB-SEM) technique to reconstruct the three-dimensional representations of the washcoat catalyst microstructure. Details are available in two submitted manuscripts [9,10].

Based on the FIB-SEM reconstructions, three-dimensional reaction-diffusion models were developed to study reaction-diffusion processes within the geometrically complex porous microstructures. The results were generalized by using a dimensionless representation of reaction and diffusion rates based on the Damkohler number [9]. The study also included a process to upscale microscale understanding to macroscale models. The approach was based on a generalization of the traditional Thiele modulus, which was directly informed by the microscale reconstructions and models [10].

References

1. S. Liu, Q. Dong, R. Ohnishi, and M. Ichikawa, "Unique promotion effect of CO and CO₂ on the catalytic stability for benzene and naphthalene production from methane on Mo/HZSM-5 catalysts". *Chem. Commun.*, 1217-1218 (1998).

2. S.L. Liu, R. Ohnishi, and M. Ichikawa, "Promotional role of water added to methane feed on catalytic performance in the methane dehydroaromatization reaction on Mo/HZSM-5 catalyst", *J. Catal.*, 220:57–65 (2003).
3. H. Ma, R. Kojima, S. Kikuchi, and M. Ichikawa, "Effective coke removal in methane to benzene (MTB) reaction on Mo/HZSM-5 catalyst by H₂ and H₂O co-addition to methane," *Catal. Lett.*, 104:63–66 (2005).
4. L. Devi and K.J. Ptasiński and F.J.J.G. Janssen, "Decomposition of naphthalene as a biomass tar over pretreated olivine: Effect of gas composition, kinetic approach, and reaction scheme," *Ind. Eng. Chem. Res.*, 44:9096-9104 (2005).
5. P. R. Buchireddy and R. M. Bricka and J. Rodriguez and W. Holmes, "Biomass gasification: Catalytic removal of tars over zeolites and nickel supported zeolites," *Energy Fuels*, 24:2707-2715 (2010).
6. Q. Wang and H. Fan and S. Wu and Z. Zhang and P. Zhang and B. Han, "Water as an additive to enhance the ring opening of naphthalene," *Green Chem.*, 14:1152-1158 (2012).
7. A. Jess, "Mechanisms and kinetics of thermal reactions of aromatics hydrocarbons from pyrolysis of solid fuels," *Fuel*, 74:1441-1448 (1996).
8. C. Karakaya, H. Zhu, R.J. Kee, "Kinetic modeling of methane dehydroaromatization chemistry on Mo/Zeolite catalysts in packed-bed reactors," *Chem. Eng. Sci.*, 123:474-486 (2015).
9. C. Karakaya, P.J. Weddle, J.M. Blasi, D.R. Diercks, and R.J. Kee, "Modeling reaction-diffusion processes within catalyst washcoats: I. Microscale processes based on three-dimensional reconstructions," *Chem. Eng. Sci.*, Submitted (2015).
10. J.M. Blasi, P.J. Weddle, C. Karakaya, D.R. Diercks, R.J. Kee, "Modeling reaction-diffusion processes within catalyst washcoats: II. Macroscale processes informed by microscale simulations," *Chem. Eng. Sci.*, Submitted (2015).

Pyrolysis kinetics and gas-phase molecular weight growth

Mario Saldana, Gregory Bogin Jr., and Anthony M. Dean

Impact of Pressure on Ethane Pyrolysis

Understanding the pyrolysis of ethane over an extended pressure range can help improve the understanding of the pressure dependence of pyrolysis of higher alkanes. For this work a variable pressure flow reactor was operated at 1073 K over pressures between 0.1 and 2.0 MPa in order to gain insight into the effect of pressure on the rate of ethane decomposition, the formation of the major products and deposit precursors like benzene and toluene. Ethane conversion was achieved by sweeping through residence times over a range from 0.2 - 30 s. The results showed that at higher pressure more ethane is converted to benzene and toluene, species which readily lead to deposit formation; additionally at elevated pressure the selectivity of hydrogen, ethylene and methane is significantly affected. The experimental results were compared to several chemical kinetic mechanisms in order to gauge the performance of the mechanisms under the various test conditions. A mechanistic analysis showed that the variation in the selectivity of the products due to pressure was due in large part by the shift in the kinetics of ethyl radicals: unimolecular β -scission dominated at lower pressures, while bimolecular addition and abstraction reactions become important at high pressures.

Introduction

Over 90 million tons of ethylene is produced yearly, making it the largest organic compound produced worldwide; ethane is the primary feedstock used to produce ethylene (Anson, 2008). Ethane is also the second most abundant species in natural gas (Foss, 2005). Additionally ethane has the potential to be used as fuel for solid oxide fuel cells (Park, 2000) (Hibino, 2000) (McIntosh, 2004). Solid oxide fuel cells, the combustion of natural gas and processing ethane into ethylene requires high temperatures; additionally these processes might operate at elevated pressure. The majority of the work on ethane pyrolysis at elevated pressure is largely composed of studies which focus on gaining an understanding of the initiation reactions at low levels of ethane conversion (Kiefer, 1129--1135) (Tranter R. S., 2002) (Tranter R. a., 2005). At higher temperatures the thermal breakdown of ethane eventually leads to the formation of carbonaceous deposits. Understanding the kinetics of molecular weight growth that occurs during the pyrolysis of alkanes is crucial in being able to implement strategies to avoid those reaction pathways that lead to deposit formation. Pyrolytic carbon deposition increases significantly at higher conversions, and this increase appears to coincide with increased production of aromatics like benzene (Glasier G. F., 2001) (Glasier G. F., 2001). A fundamental component of modeling oxidation and pyrolysis processes is the ability to accurately simulate the key chemical reactions; this is where a validated robust chemical kinetic mechanism using experimental data is essential. Xu et al. (Xu, 2011) studied ethane pyrolysis from very low conversion to conversion levels up to approximately 90%; the experiments focused on a residence time of 5 s, a pressure of ~90 kPa and a temperature range from 873-1123 K. The major products produced in the Xu et al. experiments were hydrogen, ethylene and methane, as shown in Figure 1. Reaction pathways involving vinyl and 1,3 butadiene were singled out as being particularly important in the formation of aromatics like benzene.

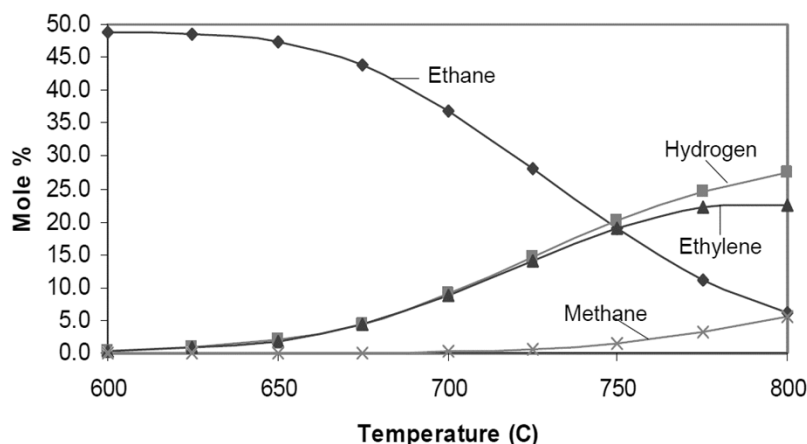


Figure 1: Concentrations of ethane, hydrogen, ethylene and methane for ethane pyrolysis Xu et al. Ethane diluted in 50% nitrogen dilution at ~90 kPa and a residence time of 5 s

The Xu et al. study characterized the kinetic behavior of ethane pyrolysis at slightly below standard atmospheric pressure. Many hydrocarbon processes such as combustion in internal combustion engines (Taylor, 1985) and within the ramjet of a supersonic aircraft (Fry, 2004) take place at significantly elevated pressure.

One of the key goals of this study is to experimentally investigate how elevated pressure affects the kinetics that govern the decomposition of ethane, the production of major products and the eventual formation of aromatic products including benzene and toluene. The data obtained in this study were compared to predictions several chemical kinetic mechanisms. This analysis showed that a shift in the reactions of the ethyl radical with pressure is important for the changing selectivity.

Experimental Description:

Ethane (Matheson gas, 99.95%) was diluted in nitrogen (Airgas, 99.998%) and delivered to a cylindrical 321 stainless steel reactor that was treated with an inert coating (SilcoTek, SilcoKlean) (Altin, 2001). For experiments at 0.1 MPa the reactor had an inner diameter of 10.9 mm and for the 2.0 MPa experiments the inner diameter was 7.04 mm. Heat for the reactor was circumferentially delivered from a 4.2 kW array consisting of 4 independently PID controlled fiber insulated heaters (Zircar ceramics, FIH type) that provided a heated length of ~100 cm at approximately constant temperature. At high pressure all reactants are delivered to a bank of mass flow controllers (Bronkhorst, F-201-AV-50K) that are calibrated for both ethane and nitrogen. The range on these mass flow controllers is 0-50 SLPM for nitrogen and 0-25 SLPM for ethane with an uncertainty of $\pm 1\%$. At 0.1 MPa and flow rates under 5 SLPM, a separate mass flow controller (Alicat Scientific, MC-5SLPM-D/5 M) was used to deliver ethane; this mass flow controller has a range of 0-5 SLPM and an uncertainty of $\pm 1\%$. Prior to being delivered to the reactor, the reactants were mixed and heated in a 675 W preheater. At the outlet of the reactor the pyrolysis products were diverted to heated exhaust lines and the sampling section.

Hydrocarbon speciation was performed using two separate Agilent 6890 GCs, one equipped with a flame ionization detector (FID) and another with a thermal conductivity detector (TCD). The FID was utilized to measure hydrocarbon species with 1-7 carbons and the TCD

was used to analyze hydrogen, nitrogen and methane. A more thorough description of the experimental setup and sampling section is provided in Saldana et al (Saldana, 2016). A schematic of the system is given in Figure 2.

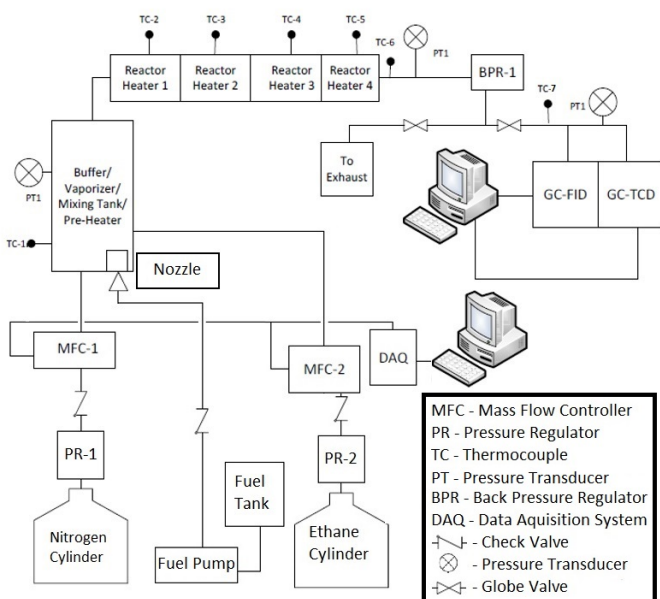


Figure 2: Schematic of the CSM variable pressure flow reactor

Modeling Description:

Modeling was done using the plug flow model in CHEMKIN-PRO (Design, 2013). The plug flow model assumes that axial diffusion is negligible relative to the flow velocity and that there exists no gradients of any kind in the radial direction. At residence times greater than 0.6 s the calculated Reynolds numbers extend into the laminar regime; this presents opportunities for wall shear and a non-uniform velocity profile. To analyze the effect of the parabolic profile on the product distribution, the cylindrical shear module in CHEMKIN-PRO (Design, 2013) was compared to the plug flow model at 0.1 and 2.0 MPa using the JetSurF 2.0 mechanism. At 0.1 MPa and a mass flow rate of 0.35 gm/s, which corresponds to a residence time of about 0.23 s, the difference in ethane conversion between the modules is approximately 7%. For the 2.0 MPa case at a mass flow of 0.21 gm/s the difference in ethane conversion between the models is approximately 6%. Figure 3 shows that difference in ethane conversion between the two models increases at higher mass flow rates.

The product selectivity of the major products methane and hydrogen are similar with both models. Therefore using the plug flow model should be adequate for exploring the effect of pressure on selectivity. For the experiments presented in this study the temperature profile was not constant. The temperature profiles were characterized over a range of conditions. The temperature along the reactor was measured by using K-type thermocouples. By analyzing various mass flow rates at pressures of 0.1 and 2.0 MPa at a fixed temperature of 1073 K it was observed that the gas temperature profile was strongly dependent on the mass flow rates but not very sensitive to the effect of pressure. For modeling, the temperature profile input used was the one that was measured for the corresponding flow condition.

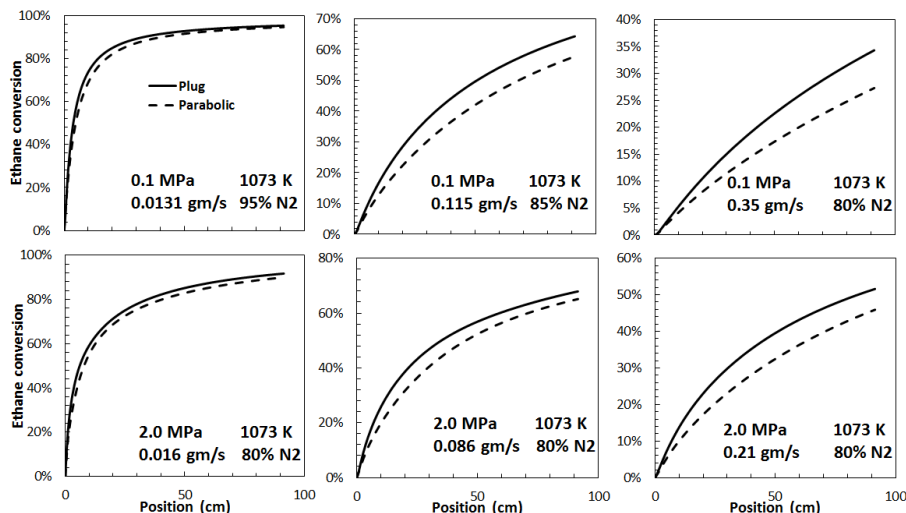


Figure 3: Comparison of the plug flow to the parabolic flow models ethane conversion vs. axial position

Since there is a mole change during pyrolysis, the kinetic model is used to calculate the residence time. The residence times include passage through the length of the reactor, including heat up and cool down regions.

For this study ethane pyrolysis experiments were conducted over a residence time from 0.2-30 s, at 1073 K and pressures of 0.1 and 2.0 MPa. The nitrogen dilution level ranged from 80-95% at 0.1 MPa and was a constant 80% at 2.0 MPa. Because varying levels of nitrogen dilution were used at 0.1 MPa, ethane conversion and the products were normalized using the following equations:

$$\overline{C_2H_6}_{converted} = 1 - \frac{x_{C_2H_6}}{\sum_i^n x_i - x_{N_2}}$$

$$\overline{X}_i = \frac{x_i}{\sum_i^n x_i - x_{N_2}}$$

where $x_{C_2H_6}$ is the mol fraction of ethane in the system, \overline{X}_i is the normalized species i , x_i is a product in the effluent, and x_{N_2} is the mol fraction of nitrogen measured at the exit.

In the following sections, the experimental data is first presented, followed by a comparison with several chemical kinetic models. Finally one of the models was used to analyze the major reaction pathways that lead to ethane decomposition, the formation of major products and the eventual the production of aromatics. The following chemical kinetic mechanisms were utilized to model the experimental data.

- The Lawrence Livermore National Laboratory (LLNL) C₁-C₄ mechanism with PAH formation. The LLNL kinetic mechanism was designed to model aromatic and PAH formation for fuel-rich, n-butane/oxygen/argon atmospheric flames and fuel-rich propane flames. The mechanism has been validated for ethane, ethylene and methane fuel-rich flames (Marinov, 1998).
- The Colorado School of Mines (CSM) mechanism. The CSM mechanism was originally developed for describing the MWG kinetics in the ethane pyrolysis at

ambient pressure (Xu, 2011), and it was recently expanded substantially to describe the pyrolysis of olefins (Wang K. a., Fundamentally-based kinetic model for propene pyrolysis, 2015). The rate constants were determined using transition state theory based on the results of electronic structure calculations, generally performed at the CBS-QB3 level of theory (Montgomery Jr, 1999), or from reliable experiments whenever available. The QRRK/MSM approach (Chang, 2000) was used to analyze the impact of pressure for the pressure-dependent reactions in the mechanism.

- The CRECK C₁-C₃ mechanism (Version 1412, December 2014). The mechanism was developed for pyrolysis, partial oxidation and combustion of hydrocarbon fuels up to 3 carbon atoms (Ranzi, 2012).
- The JetSurF 2.0 mechanism. The JetSurF model 2.0 resulted from an extensive collaboration among many institutions, and was centered on combustion kinetics for both small and large hydrocarbons. For some reactions in the JetSurF model, theoretical calculations were performed to obtain the high pressure limit rate constants and to analyze the pressure-dependence. For the rest of the reactions, estimation techniques based on similar reaction analogies were used to get the rate parameters (Wang H. a., 2010).

Experimental results:

This section presents the experimental results for ethane pyrolysis at 0.1 and 2.0 MPa. The measured carbon and hydrogen balances; at both pressures these were within $\pm 4\%$. The results of ethane conversion as a function of residence time are presented in Figure 4. The most striking observation from this plot is the difference in time it takes for ethane to convert to products at the two pressures. Although the time required to reach comparable conversions is about 5 times longer at 2.0 MPa, the rate of ethane concentration decay is actually about 4 times higher at 2.0 MPa due to the concentration being approximately 20 times higher.

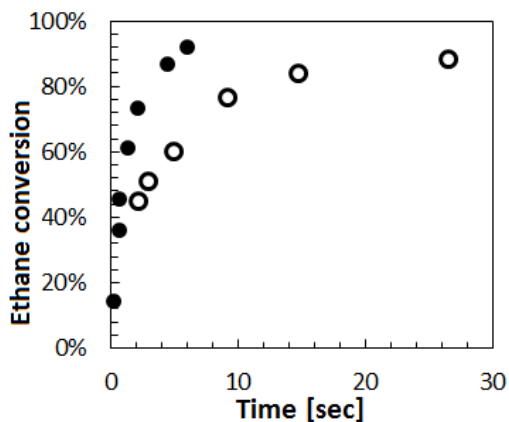


Figure 4: Ethane conversion vs. residence time at 0.1 (●) and 2.0 MPa (○) at 1073 K

Figure 5 shows the impact of pressure on selectivity of the major species; additionally the plots compare the data to that of Xu et al. (Xu, 2011). Over the range of conditions tested the major species produced were hydrogen, methane and ethylene; for these species pressure impacts selectivity at ethane conversion levels greater than $\sim 40\%$. While hydrogen and ethylene selectivity decrease at higher conversions, the opposite is true for methane.

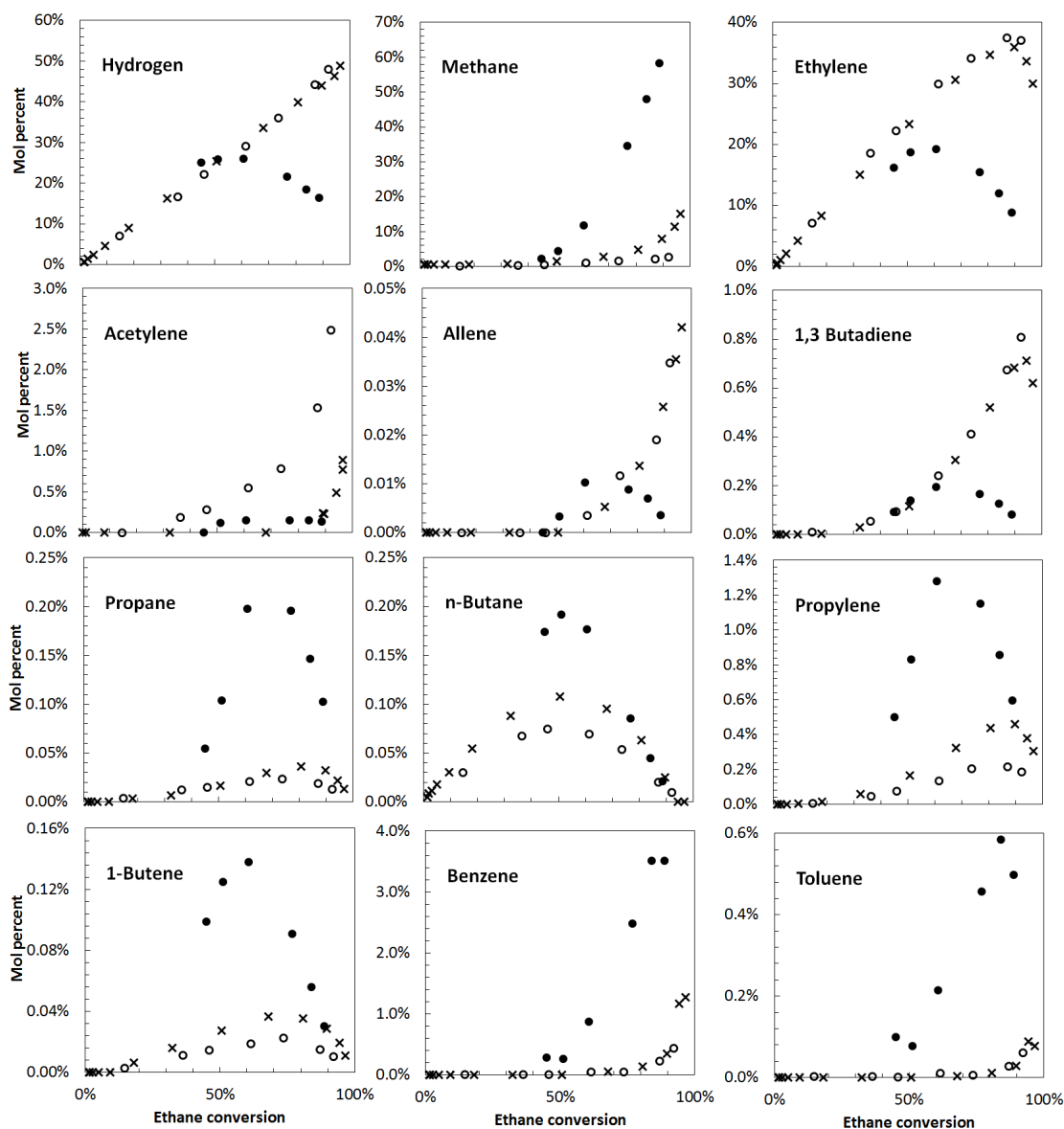


Figure 5: Hydrogen, methane, ethylene, acetylene, allene, 1,3 butadiene, propane, n-butane, propylene, 1-butene, benzene and toluene mol percent vs. ethane conversion. 0.1 MPa (□) with 80-95% nitrogen dilution and 2.0 MPa (○) with 80% dilution at 1073 K over a residence time range from 0.2 – 30 s. Xu et al. at ~90 kPa (x), residence time 5s and temperature range from 823-1123 K with 50% nitrogen dilution.

At higher pressure the selectivity of minor species like propane, n-butane, propylene and 1-butene also increase; these species also exhibit maxima that reach higher concentrations at elevated pressure. Similar to hydrogen and ethylene; acetylene, allene, and 1,3 butadiene selectivity is inhibited by an increase in pressure. At increased pressure the selectivity of benzene and toluene substantially increase. Similar to the major species, the departure from low pressure behavior occurred at ethane conversion levels greater than ~40%.

As was mentioned in the introduction, Xu et al. (Xu, 2011) carried out ethane pyrolysis experiments where ethane conversion was accomplished by varying temperature at a fixed residence time and pressure. Figure 5 compares the selectivity of the major products for the Xu et al. (Xu, 2011) study with the experiments conducted in this work. Although the current

work varied residence time at a fixed temperature, the selectivity for the major products, with the exception of acetylene, is remarkably close, indicating that the selectivity is more influenced by pressure effects than temperature and residence time; these results are consistent with the n-pentane pyrolysis experiments that were performed by Saldana et al. (Saldana, 2016).

The most important observations from the experimental results are the change in selectivity of the major products with pressure begins at ethane conversion levels above 40%. The decrease in ethylene and hydrogen at higher pressure may be the reason why acetylene, allene, and 1,3 butadiene are also suppressed.

Kinetic analysis:

The first comparison shown is for ethane conversion as a function of residence time at 0.1 and 2.0 MPa. Figure 6 show that all the models do a reasonable job at predicting experimental trends for ethane conversion in the two pressure regimes. At 0.1 MPa the models over predict the initial decomposition rate. The CSM and CRECK models best capture the decomposition rate of ethane at 0.1 MPa. At 2.0 MPa the CSM model best predicts ethane conversion while the other models tend to under predict the experimental data at later times. The reason for the deviations in ethane conversion observed may be due to the differences between the plug flow and parabolic flow models. Note in Figure 3 that the parabolic model predicts a slower conversion rate. Although there were differences between the mechanisms for ethane conversion it was shown in the modeling section that the models were very similar in predicting selectivity, which means that the plug flow module should be adequate in modeling the observed experimental selectivity.

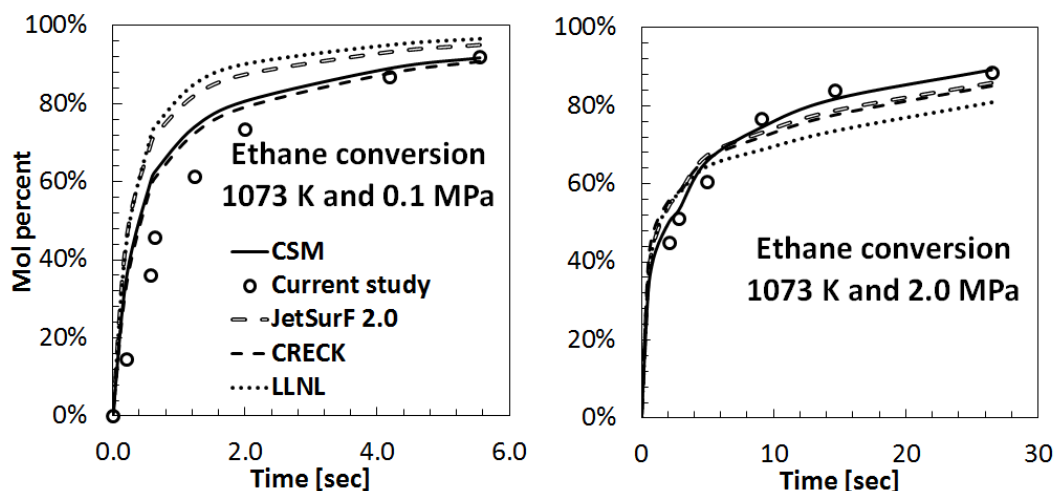


Figure 6: Comparison of experiment to chemical kinetic models of ethane conversion vs. residence time at 0.1 and 2.0 MPa and at 1073 K

Selectivity of major products at 0.1 and 2.0 MPa was compared for the various chemical kinetic mechanisms. Figure 7 compares the predictions to the experimental results for hydrogen, ethylene and methane. At 0.1 MPa the agreement is very good for hydrogen and ethylene. For methane agreement is good up to ethane conversion levels of 75% at which point the mechanisms predict a more rapid increase in selectivity than observed. At 2.0 MPa the mechanisms better capture the experimental data for methane, which is important since

methane is the dominant product. The models show good agreement with one another at conversion levels up to about 40% for hydrogen, methane and ethylene; at higher levels of conversion the models capture the overall trends but begin to show some variance. The overall reasonable predictions are encouraging but not surprising since the most important reactions for production of these species are quite well characterized.

Figure 8 compares the experimental data for acetylene, 1,3 butadiene, propylene and 1-butene to the predictions. Unlike predictions for the major species, the selectivity predictions with the various mechanisms vary widely. At 0.1 MPa all of the mechanisms capture the overall trends for increasing acetylene at higher conversions but tend to under predict the actual concentration; this is also true at 2.0 MPa with the exception of the JetSurF mechanism, which over predicts acetylene. For 1,3 butadiene, at 0.1 and 2.0 MPa the CSM mechanism predicts the experimental data reasonably well, while the LLNL mechanism appears to substantially over predict the results at 2.0 MPa. The CSM and JetSurF mechanisms do a fair job at predicting the trends observed in propylene and 1-butene at both 0.1 and 2.0 MPa.

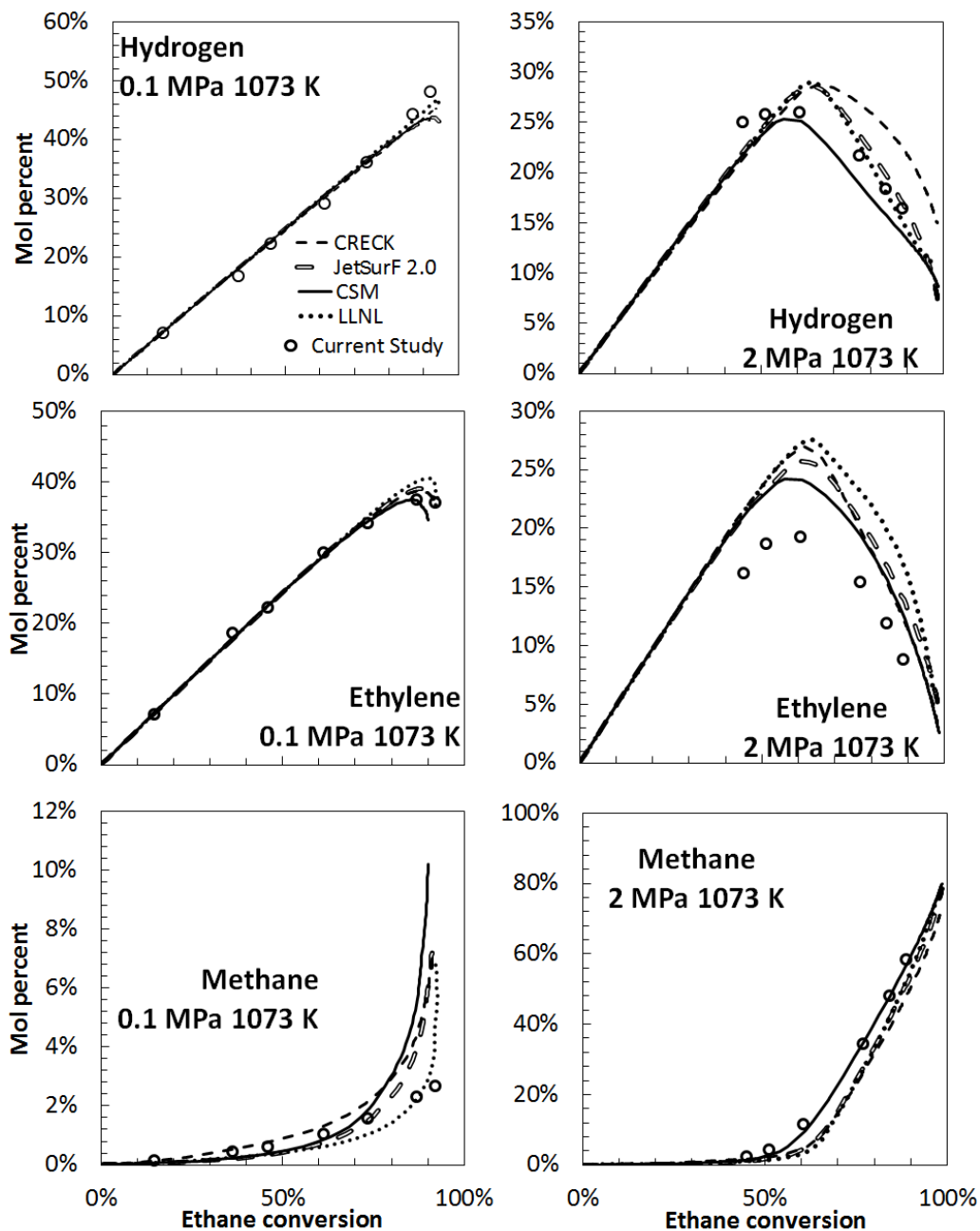


Figure 7: Comparison of experiment to chemical kinetic models of hydrogen, ethylene and methane mol percent vs. ethane conversion at 0.1 (with 80-95% nitrogen dilution) and 2.0 MPa (with 80% dilution) at 1073 K over a residence time range 0.2-30s.

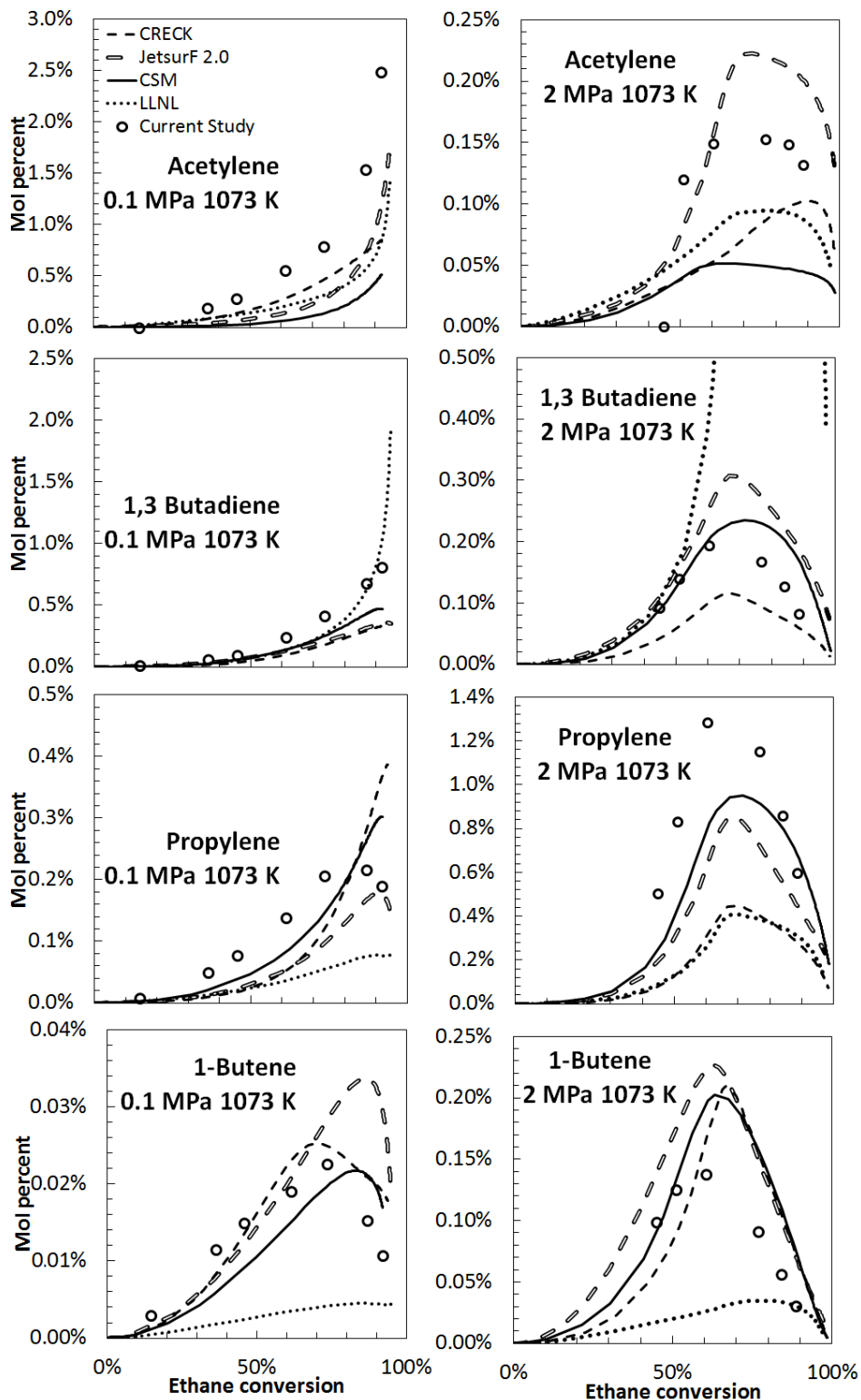


Figure 8: Comparison of experiment to chemical kinetic models of acetylene, 1,3 butadiene, propylene and 1-butene mol percent vs. ethane conversion at 0.1 (with 80-95% nitrogen dilution) and 2.0 MPa (with 80% nitrogen dilution) at 1073 K over a residence time range 0.2-30 s.

The comparisons for benzene and toluene are shown in Figure 9 (the CRECK model did not include toluene). For these species there is significant variance between the models; overall the CSM mechanism did best at predicting the experimental data observed for these aromatics, especially for the 0.1 MPa case. The CSM mechanism also captured the large selectivity increase to benzene and toluene at 2.0 MPa.

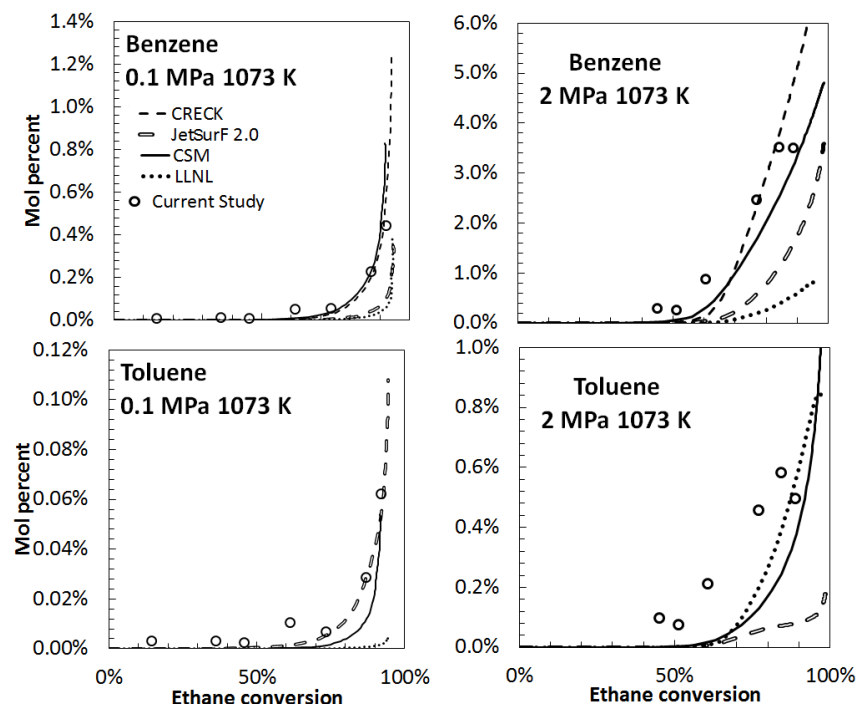


Figure 9: Comparison of experiment to chemical kinetic models of benzene and toluene mol percent vs. ethane conversion at 0.1 (with 80-95% nitrogen dilution) and 2.0 MPa (with 80% nitrogen dilution) at 1073 K over a residence time range 0.2-30 s.

In this section it was observed that the selectivity of the major species had strong pressure dependence; all models did a good job at predicting the trends observed in the major species hydrogen, ethylene and methane. The comparison of the results for the minor species was not as consistent. Although there are discrepancies, the CSM model appears to better describe the effect of pressure for the olefins and aromatics, species which have been identified as deposit precursors.

Discussion

A sensitivity and rate of production analysis was carried out to gain insight into the chemistry dominating ethane decomposition, the formation of major products and the eventual formation of aromatics. This analysis was done in CHEMKIN-PRO (Design, 2013) using the CSM mechanism.

The sensitivity analysis presented in Table 1 is for ethane at 0.1 MPa at varying levels of conversion. This analysis revealed that at low pressure ethane decomposition is only sensitive to a few well-characterized reactions. The sensitivity to only to a few reactions explains why the model predictions did so well at low pressure, since these reactions are well studied

(Slagle, 1988) (Wardlaw, 1986) (Robertson, 1993) (Oehlschlaeger, 2005). At 0.1 MPa the reaction which is most important for ethane decomposition is the hydrogen abstraction from ethane by H-atoms, R(2), but note at higher conversion this reaction is becoming partially equilibrated resulted in significantly smaller sensitivity. The sensitivity analysis also showed that R(1), the decomposition of ethane to methyl radicals is important at mid and high conversion. At mid conversion the β -scission of ethyl, R(3) is important, but as conversion progresses this reaction becomes equilibrated.

Table 1: Sensitivity coefficients for ethane at 0.1 MPa, 1073 K and varying levels of conversion taken at the end of the reactor

	Ethane conversion	57.66%	91.62%
R(1)	$C_2H_6(+M) \rightarrow 2CH_3(+M)$	-0.14	-0.15
R(2)	$C_2H_6 + H \rightarrow C_2H_5 + H_2$	-0.23	-0.66
R(-2)	$C_2H_5 + H_2 \rightarrow C_2H_6 + H$	0.03	0.58
R(3)	$C_2H_5(+M) \rightarrow C_2H_4 + H(+M)$	-0.24	-0.61
R(-3)	$C_2H_4 + H(+M) \rightarrow C_2H_5(+M)$	0.11	0.61

The rate of production analysis in Figure 10: Rate of production analysis for ethane at 0.1 MPa and 1073 K, Left: Function of time. Right: Function of ethane conversion is for ethane at 0.1 MPa. This analysis shows that by far most ethane is consumed by H-atoms abstracting hydrogen from ethane, R(2). The majority of H-atoms that are responsible for ethane decomposition are generated through the β -scission of ethyl, R(3). The dominance of this reaction explains why ethylene and hydrogen are the major products for ethane pyrolysis at 0.1 MPa.

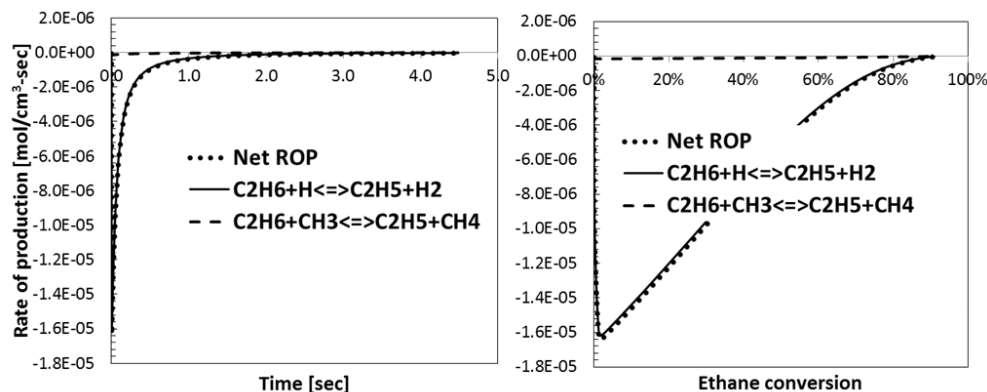


Figure 10: Rate of production analysis for ethane at 0.1 MPa and 1073 K, Left: Function of time. Right: Function of ethane conversion

A sensitivity and rate of production analysis was also done for ethane at 2.0 MPa and 1073 K, the results are shown in Table 2 and Figure 11. The sensitivity analysis in Table 2 shows that at elevated pressure ethane decomposition is not as sensitive to H-atoms abstracting hydrogen from ethane, R(2), since this reaction appears to equilibrate early on. The main source of H-atoms, R(3) also equilibrates early on. Instead, at higher levels of ethane conversion, ethane decomposition is much more sensitive to hydrogen abstractions by methyl, reaction R(4). The sensitivity analysis at 2.0 MPa also highlighted that at high conversion the decomposition of ethane is more sensitive to chemistry involving olefins like propylene and 1-butene, reactions R(5)-R(7).

Table 2: Sensitivity coefficients for ethane at 2.0 MPa, 1073 K and varying levels of conversion taken at the end of the reactor

	Ethane conversion	57.89%	91.61%
R(1)	$C_2H_6(+M) \rightarrow 2CH_3(+M)$	-0.09	-0.34
R(2)	$C_2H_6 + H \rightarrow C_2H_5 + H_2$	-0.27	-0.41
R(-2)	$C_2H_5 + H_2 \rightarrow C_2H_6 + H$	0.23	0.39
R(3)	$C_2H_5(+M) \rightarrow C_2H_4 + H(+M)$	-0.24	-0.30
R(-3)	$C_2H_4 + H(+M) \rightarrow C_2H_5(+M)$	0.22	0.30
R(4)	$C_2H_6 + CH_3 \rightarrow C_2H_5 + CH_4$	-0.03	-0.27
R(-4)	$C_2H_5 + CH_4 \rightarrow C_2H_6 + CH_3$	0.01	0.19
R(5)	$C=CCC(+M) \rightarrow C=CC + CH_3(+M)$	-0.05	-0.20
R(6)	$C=CC + C_2H_5(+M) \rightarrow C_2.CCC(+M)$	-0.04	-0.26
R(7)	$C=CC + C_2H_5(+M) \rightarrow C=CCC + CH_3(+M)$	-0.02	-0.17

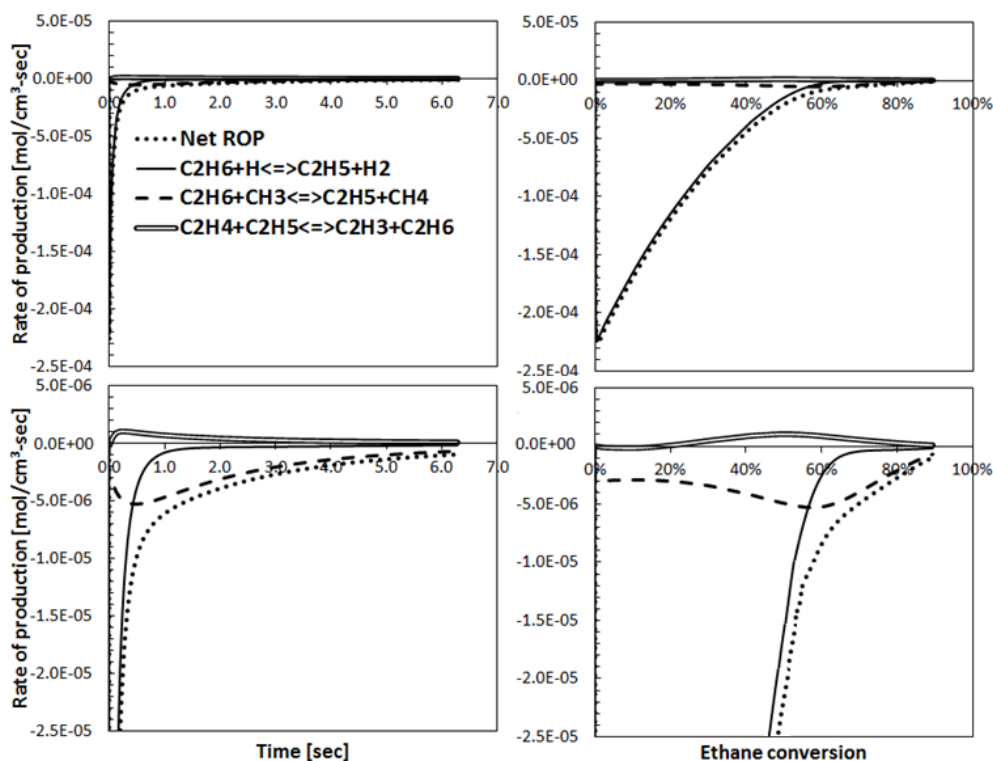
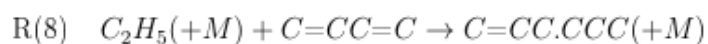


Figure 11: Rate of production analysis for ethane at 2.0 MPa and 1073 K. Left: as a function of time. Right: as a function of ethane conversion. Bottom: Plots have an expanded y-axis.

The rate of production analysis for ethane at 2.0 MPa in Figure 11 shows that initially, similar to the 0.1 MPa rate of production analysis, ethane decomposition is being driven by H-atoms abstracting hydrogen from ethane. A key difference is that as conversion progresses hydrogen abstractions by H-atoms are overtaken by abstractions by methyl radicals. This observation helps explain why at 2.0 MPa, at higher conversion there is less hydrogen and more methane produced.

Thus far it has been shown that H-atoms, methyl and ethyl are important radical species in the decomposition of ethane. Of these radicals, ethyl is the only one which both unimolecular β -scission, R(3), and bimolecular reactions, e.g. R(-4) and R(7) may occur. Since unimolecular reactions scale linearly with pressure (at high pressure limit) and bimolecular reactions scale with the square of the pressure, the reactions of ethyl could explain the large changes in selectivity with pressure. A rate of production analysis for ethyl is presented in Figure 12. The analysis shows that at 0.1 MPa, ethyl radical formation is driven by H-atoms abstracting from ethane to form ethyl radicals and primarily being consumed by the unimolecular β -scission of ethyl radicals. At 2.0 MPa the rate of production analysis shows that initially the same formation and consumption pathways dominate; however as conversion progresses ethyl is being primarily formed by methyl abstracting hydrogen from ethane and being consumed by the bimolecular reactions like, R(8).



A major difference is that at this higher pressure and later times ethyl radicals now begin to react with other species before they can β -scission. These shifts in the behavior of ethyl lead to a decrease of H-atoms produced via β -scission.

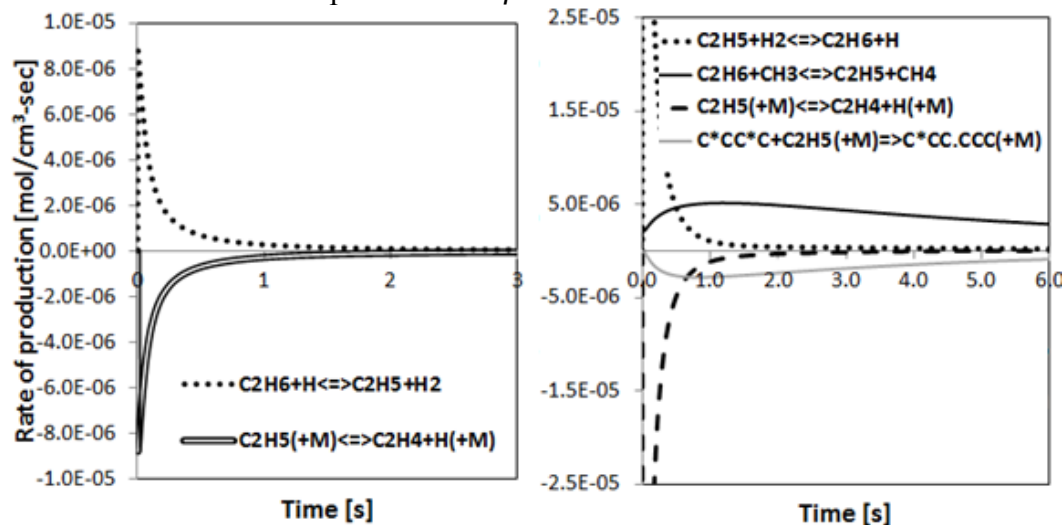
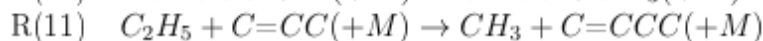
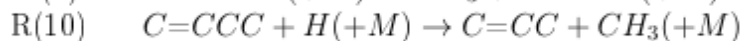
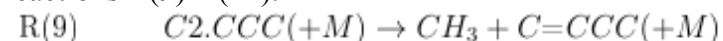


Figure 12: Left: rate of production analysis for ethyl at 0.1 MPa and 1073 K. Right: rate of production analysis for ethyl at 2.0 MPa and 1073 K.

Bimolecular reactions like, reaction R(8) lead to larger allylic and alkyl species; these alkyl species undergo decomposition lead to the production of methyl radicals and olefins, e.g. reactions R(9)-R(11).



The formation of C₃⁺ olefins is important in the generation of benzene and toluene because they lead to production of cyclic dienyl species. Olefins readily produce allylic radicals and these allylic radicals are much more stable than alkyl radicals which make them less reactive and lead to their accumulation, which also leads to a less reactive system. At elevated pressure there is an increase in the presence of allylic radicals, these allylic radicals through addition reactions lead to the formation of larger dienes and dienyl species, species which undergo

cyclization to form cyclic dienes. These cyclic dienes like cyclohexadiene have pathways that readily lead to the production of aromatics (Wang K. a., Reactions of allylic radicals that impact molecular weight growth kinetics, 2015).

Conclusion

In this work a variable pressure flow reactor was utilized to investigate ethane pyrolysis at 1073 K at pressures of 0.1 and 2.0 MPa over a residence time range from 0.2-30 s. The experimental data were compared to existing chemical kinetic mechanisms in order to gauge the performance of these mechanisms over an extended pressure range. The mechanisms were able to accurately describe the major features of ethane pyrolysis but predictions varied for many of the minor species which are important in the formation of molecular weight growth products like benzene and toluene. A chemical kinetic analysis was carried out by means of a sensitivity and rate of production analysis. The analysis revealed that at elevated pressure there is a significant shift in the reactions dominating ethane pyrolysis with a corresponding shift in product selectivity. A significant finding was that at elevated pressure more ethane was converted to aromatics; additionally higher olefins like propylene and 1-butene attained greater maximums. The analysis found that at elevated pressure bimolecular reactions competed with unimolecular reactions. The increased presence of allylic radicals is believed to be the primary reason for more ethane being converted into aromatic species at elevated pressure under the conditions tested.

References

- Altin, O. et al. (2001). Analysis of solid deposits from thermal stressing of a JP-8 fuel on different tube surfaces in a flow reactor. *Industrial & engineering chemistry research* , 596-603.
- Anson, A. et al. (2008). Adsorption of ethane and ethylene on modified ETS-10. *Chemical Engineering Science* , 4171--4175.
- Chang, A. et al. (2000). Kinetic analysis of complex chemical activation and unimolecular dissociation reactions using QRRK theory and the modified strong collision approximation. *Physical Chemistry Chemical Physics*, 1533.
- Chemkin-Pro Release 15131. (2013) *Reaction Design, San Diego, CA* .
- Foss, M. M. et al. (2005). Introduction to LNG. *Center for Energy Economics, Bureau of Economic Geology, Jackson School of Geosciences, University of Texas, Austin, TX.[Online]. Available: http://www.beg.utexas.edu/energyecon/lng/documents/CEE_INTRODUCTION_TO_LNG_FINAL.pdf*, 1129-1135.
- Fry, R. S. (2004). A century of ramjet propulsion technology evolution. *Journal of propulsion and power* , 27--58.
- Glasier, G. F. et al. (2001). Formation of polycyclic aromatic hydrocarbons coincident with pyrolytic carbon deposition. *Carbon* , 497-506.
- Glasier, G. F. et al. (2001). Formation of pyrolytic carbon during the pyrolysis of ethane at high conversions. *Carbon* , 15-23.
- Hibino, T. et al. (2000). A low-operating-temperature solid oxide fuel cell in hydrocarbon-air mixtures. *Science* , 2031-2033.

Kiefer, J. et al. (2005). Dissociation, relaxation, and incubation in the high-temperature pyrolysis of ethane, and a successful RRKM modeling. *Proceedings of the Combustion Institute*, 1129-1135.

Marinov, N. M. et al. (1998). Aromatic and polycyclic aromatic hydrocarbon formation in a laminar premixed n-butane flame. *Combustion and flame*, 192-213.

McIntosh, S. et al. (2004). Direct hydrocarbon solid oxide fuel cells. *Chemical reviews*, 4845-4866.

Montgomery Jr, J. A. et al. (1999). A complete basis set model chemistry. VI. Use of density functional geometries and frequencies. *The Journal of chemical physics*, 2822-2827.

Oehlschlaeger, M. A. et al. (2005). High-temperature ethane and propane decomposition. *Proceedings of the Combustion Institute*, 1119-1127.

Park, S. (et al. 000). Direct oxidation of hydrocarbons in a solid-oxide fuel cell. *Nature*, 265--267.

Ranzi, E. et al. (2012). Hierarchical and comparative kinetic modeling of laminar flame speeds of hydrocarbon and oxygenated fuels. *Progress in Energy and Combustion Science*, 468-501.

Robertson, S. et al. (1993). Potential energy function for $\text{CH}_3 + \text{CH}_3 = \text{C}_2\text{H}_6$: Attributes of the minimum energy path. *The Journal of chemical physics*, 7748-7761.

Saldana, M. H. et al. (2016). Investigation of n-pentane pyrolysis at elevated temperatures and pressures in a variable pressure flow reactor. *Journal of Analytical and Applied Pyrolysis*, 286--297.

Slagle, I. R. et al. (1988). Study of the recombination reaction methyl+ methyl. fvdarw. ethane. 1. Experiment. *The Journal of Physical Chemistry*, 2455-2462.

Taylor, C. F. (1985). *The Internal-combustion Engine in Theory and Practice: Combustion, fuels, materials, design*. MIT press.

Tranter, R. S. et al. (2005). Ethane oxidation and pyrolysis from 5 bar to 1000 bar: Experiments and simulation. *International journal of chemical kinetics*, 306-331.

Tranter, R. S. et al. (2002). High pressure, high temperature shock tube studies of ethane pyrolysis and oxidation. *Physical Chemistry Chemical Physics*, 2001-2010.

Wang, H. et al. (2010). A high temperature chemical kinetic model of n-alkane (up to n-dodecane), cyclohexane, and methyl-, ethyl-, n-propyl and n-butyl-cyclohexane oxidation at high temperatures, JetSurF version 2.0; September 19, 2010. URL: <http://melchior.usc.edu/JetSurF/JetSurF2.0>.

Wang, K. et al. (2015). Fundamentally-based kinetic model for propene pyrolysis. *Combustion and Flame*, 4456-4470.

Wang, K. et al. (2015). Reactions of allylic radicals that impact molecular weight growth kinetics. *Physical Chemistry Chemical Physics*, 6255-6273.

Wardlaw, D. M. et al. (1986). Unimolecular reaction rate theory for transition states of any looseness. 3. Application to methyl radical recombination. *The Journal of Physical Chemistry*, 5383-5393.

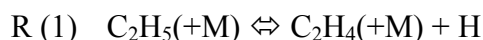
Xu, C. et al. (2011). Kinetic modeling of ethane pyrolysis at high conversion. *The Journal of Physical Chemistry A*, 10470-10490.

Pyrolysis of *n*-Pentane and *n*-Hexane

n-Pentane pyrolysis experiments were carried out at pressures of 0.1 and 2.0 MPa. *n*-Pentane (Sigma Aldrich, 99%) was diluted in 11-19% nitrogen (Airgas, 99.999%). Conversion of *n*-pentane was accomplished in two ways, one by adjusting residence time at a fixed temperature and pressure and also by adjusting temperature over a range from 923-1073 K at a fixed residence time and pressure. At 0.1 MPa for the residence time sweep experiments at 1073 K it takes ~400 ms to convert ~90% of the fuel, while at 2.0 MPa it takes longer than 500 ms to get to the same level of conversion. *n*-Hexane experiments were done at a 0.1 and 2.0 MPa. For these experiments *n*-hexane (Sigma-Aldrich, > 99%) was diluted in ~80% nitrogen (Airgas, 99.999%). Similarly to *n*-pentane, conversion was achieved by adjusting residence time at a fixed temperature and pressure; conversion was also achieved by sweeping through temperature over range from 923-1073 K at a fixed pressure and residence time. At 0.1 MPa and 1073 K *n*-hexane conversions ranged from ~21-94% over a residence time from 20-90 ms, while at 2.0 MPa and 1073 K conversions ranged from ~6-96% over a residence time range from 200-700 ms.

Figure 13 shows the major products for both *n*-pentane and *n*-hexane pyrolysis as a function of fuel conversion. The impact of pressure on observed selectivities are very similar for both fuels. Similar to ethane pyrolysis, elevated pressure results in a decrease in ethylene and hydrogen selectivities but unlike ethane pyrolysis the effect of pressure on hydrogen production is greater than the effect on ethylene.

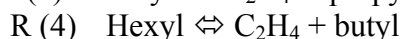
This behavior and the behavior of the other species can be explained by revisiting the major chemical pathways that were most affected by pressure for ethane pyrolysis. It was shown in the ethane section that the unimolecular β -scission of ethyl, R (1) played a large part in the pressure effects observed for ethane pyrolysis. The β -scission of ethyl is a major source of H-atoms; these H-atoms then go on to abstract hydrogen from other molecules to form hydrogen molecules.



At elevated pressure ethyl carries out hydrogen abstractions on other molecules to form ethane, R (2).



This shift in the behavior of ethyl explains why there is much less hydrogen and much more ethane produced at higher pressure for *n*-pentane and *n*-hexane pyrolysis. Ethylene was not as affected by pressure for *n*-pentane and *n*-hexane pyrolysis as it was for ethane pyrolysis. For ethane the R (1) shown to be the major production channel for ethylene. For *n*-pentane and *n*-hexane pyrolysis reaction R(1) is also a dominant channel for the production of ethylene but there also exists other channels where larger radicals undergo β -scissions to produce ethylene plus an alkyl, R(3) and R (4).



The alkyl radicals created in R (3) and R (4) can also undergo β -scissions which lead to smaller alkyl radicals and additional ethylene. The breakdown of higher alkyl radicals

eventually leads to the production of methyl radicals that then lead to the formation of methane.

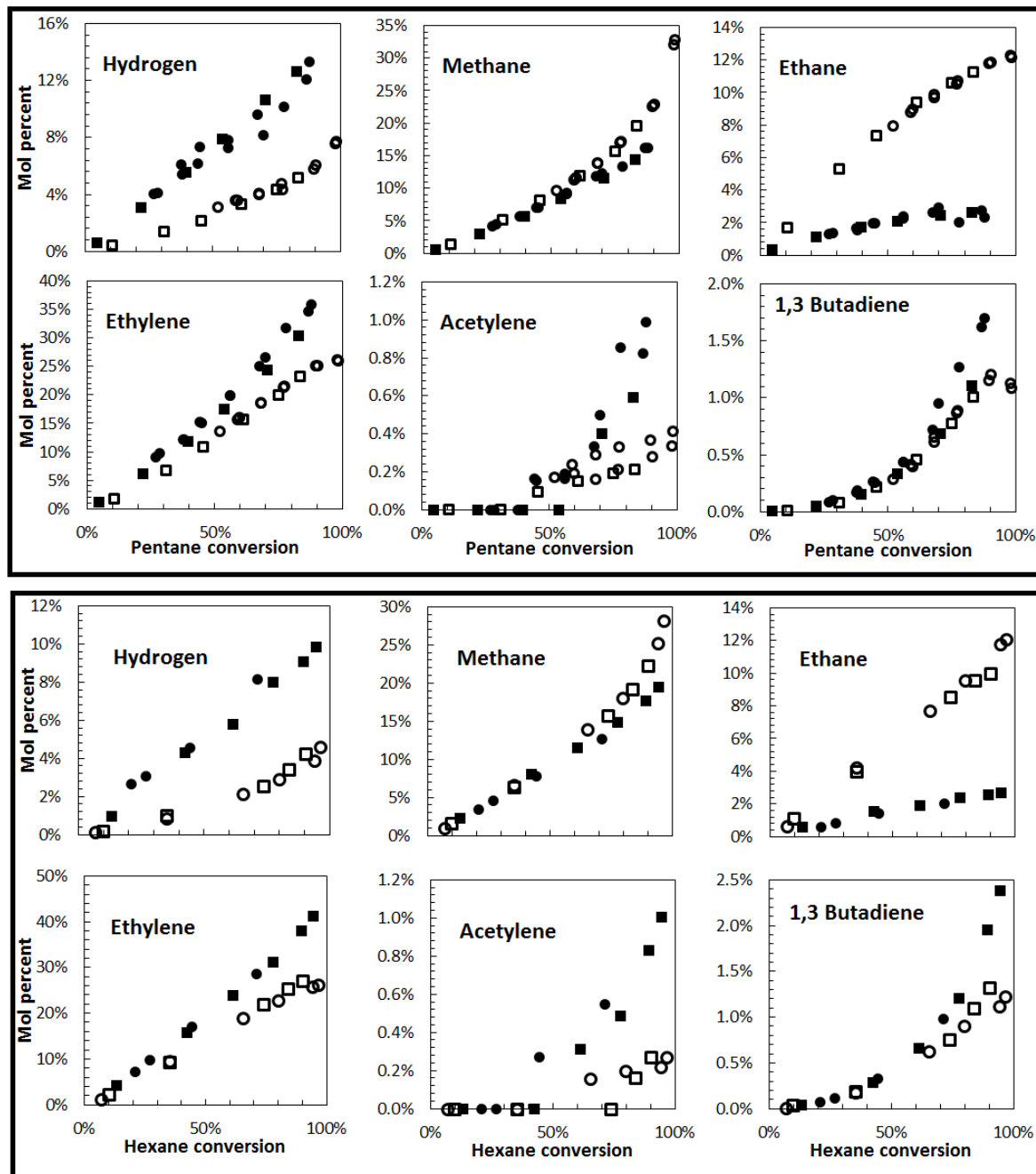


Figure 13: Top: Major products for n-pentane pyrolysis. Bottom: Major products for n-hexane pyrolysis. 0.1 MPa time sweep (closed circle) 0.1 MPa temperature sweep (closed square) 2.0 MPa residence temperature sweep (open square) 2.0 MPa residence time sweep (open circle)

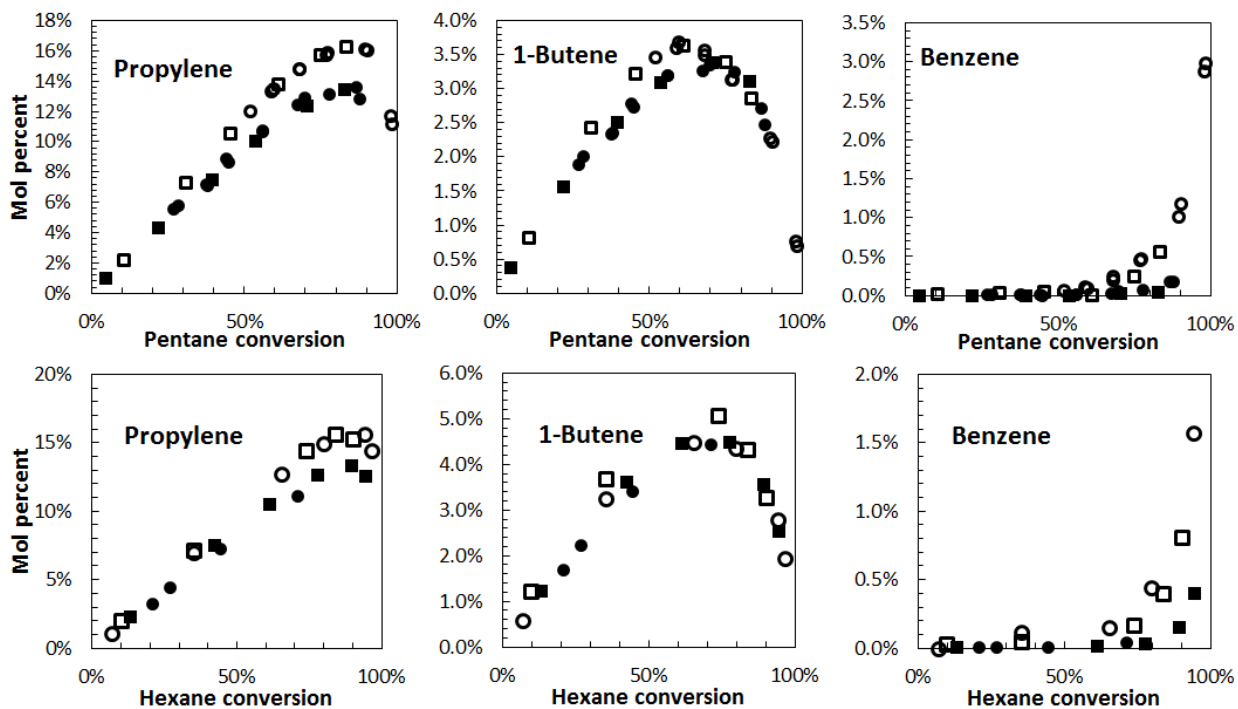


Figure 14: Top: Propylene, 1-butene and benzene for n-pentane pyrolysis. Bottom: Propylene, 1-butene and benzene for n-hexane pyrolysis. 0.1 MPa time sweep (closed circle) 0.1 temperature sweep (closed square) 2.0 MPa residence temperature sweep (open square) 2.0 MPa residence time sweep (open circle)

One major difference from the ethane pyrolysis experiments is the higher selectivity to propylene and 1-butene. Figure 14 highlights that propylene is one of the species produced in greatest concentrations. At elevated pressure the selectivity for propylene and benzene increases, while for 1-butene it appears to remain the same. The observed maxima for propylene and butane suggest these species are involved in the reactions that lead to increased molecular weight growth. These data are especially important in the context of validating the pressure dependence of detailed kinetic mechanisms, as demonstrated above for ethane pyrolysis.

United Technologies Research Center

Heterogeneously Catalyzed Endothermic Fuel Cracking

Susanne Opalka, Tianli Zhu, He Huang

Executive Summary

The research contributions from the United Technologies Research Center (UTRC) focused on the design of aluminosilicate zeolite-based catalyst model systems for enhanced supercritical hydrocarbon fuel endothermic conversion using combined experimental–theoretical methodologies, encompassing catalyst modification {calcination, noble metal and alkali metal exchange}, specially tailored real-time spectroscopic catalytic reactor studies {in situ cylindrical internal reflectance–Fourier transform infrared spectroscopy/gas chromatography (CIR–FTIR/GC)} with *n*-pentane and *n*-heptane surrogate hydrocarbon fuel molecules, catalyst characterization {temperature programmed desorption–mass spectrometry (TPD-MS) with the basic isopropylamine (IPA) probe molecule, temperature programmed oxidation (TPO), along with additional complementary characterizations conducted by Prof. Raul Lobo’s group at the University of Delaware (UD)}, and atomic modeling of catalyst properties and fuel conversion reactions {Towhee code [1] grand canonical Monte Carlo (GCMC), VASP code [2] density functional theory with periodic basis}. The H-[Al]ZSM-5 and H-[Al]Beta commercial zeolites with 3-D pore networks and varying Si/Al ratios were selected as model catalyst systems, in collaboration with UD. The research progressively surveyed across a multi-dimensional design space for the balancing zeolite catalytic site functionality for enhanced endothermic cracking and dehydrogenation to increase light olefin yield and selectivity with minimized coke precursor formation and site deactivation. The survey benchmarked and refined zeolite multi-functionality in a series of phases, summarized in Table 1, including: I) zeolite framework type and Si/Al ratio influence on intrinsic Brønsted acid site fuel cracking functionality, II) incorporation of extrinsic Pt sub-nanometric sites for introducing bi-functional fuel activation and dehydrogenation functionality, and III) Brønsted acid site titration by exchange with Cs modifiers to alter balance of bi-functional reaction mechanisms. In culmination, the UTRC heat exchanger rig was used to measure *n*-dodecane conversion endotherms catalyzed by two catalyst candidates selected by the Utah and Colorado School of Mines AFOSR Endothermic BRI teams.

Table 1. Summary of multi-functional zeolite design space.

Zeolite Reaction Site Type	Structural Features	Reaction Selectivity	Reaction Functionality
Intrinsic	-framework topography -Si/Al ratio	site turnover Brønsted acid cracking	-mixed olefin/alkane cracked products, -turnover by chain propagation, -oligomerized & cyclized side-products
Extrinsic	-sub-nanometric Pt clusters -mode of Pt incorporation	dehydrogenation	-increased olefin production, -activation for forming acid carbenium, -cracking without chain propagation
Promoter/ Modifier	% exchange Cs alkali metal	acid site titration Lewis acid/base	-block oligomerization and cyclization -moderate Brønsted & Pt reactivity

1.0 CIR–FTIR/GC Studies

1.1 *n*-Pentane cracking on H-ZSM-5 and Beta

The primary objective was to study the catalytic cracking of supercritical *n*-pentane inside the H-ZSM-5 and Beta zeolites, using an annular, packed bed, cylindrical internal reflectance–Fourier transform infrared (CIR–FTIR) reactor coupled with gas chromatography (GC) product analyses. The H-ZSM-5 and Beta selected for testing under supercritical *n*-pentane

conditions had similar Si/Al ratios and comparable Brønsted acid site densities. In addition to measuring the *n*-pentane conversion and change in catalyst activity as a function of time, the CIR–FTIR was used to measure changes in situ reaction intermediates on the catalyst surface with time in the supercritical *n*-pentane environment. The operating temperature of 450 °C corresponded to the upper temperature limit of the ZnSe crystal used in CIR–FTIR.

The in situ CIR–FTIR spectra showed the formation of aromatic and olefinic species on the zeolite catalyst during supercritical *n*-pentane cracking. These surface species appeared to form the catalyst surface within a very short time on stream, followed by little subsequent change afterwards. Fig. 1 shows the change in the Fourier transform infrared (FTIR) spectra of *n*-pentane cracking intermediates on H-ZSM-5 with time, under the 450 °C and 60 bar *n*-pentane supercritical conditions. The *n*-pentane reactant flow was 9.5 ml/min, corresponding to a residence time of 1 s under the reaction conditions. The intensity of the band at 1600 to 1550 cm⁻¹, assigned to the formation of olefinic and aromatic species on catalyst surface (see Table 2), had a rapid initial increase, and then showed very little change after ~39 min on stream. The GC results showed that the pentane conversion decreased initially, then stabilized at around 40 to 58 minutes on stream, as shown in Fig. 2. The conversion decreased from 28.3% at 21 min to 23.5% at 58 min, an overall 17% decrease in activity. These results suggest that the surface olefinic and aromatic species were causing the deactivation of the H-ZSM-5 catalyst and that the catalyst activity stabilized as the formation of the surface species reached a steady state. This may have been due to the balance between carbon deposition and the removal of carbon and carbon precursors by the supercritical *n*-pentane.

Table 2. Assignment of major FTIR bands during *n*-pentane cracking on zeolite catalysts.

FTIR wavenumbers (cm ⁻¹)	Band assignment
3000–2800	Pentane C–H stretch
1390 & 1450	Pentane C–H bend, C–C stretch of aromatic ring
1650–1585	C=C stretch of olefins, C–C stretch of aromatic ring
2000–1665	Aromatic ring overtone

At a lower supercritical *n*-pentane pressure, i.e., 34 bar, more aromatic and olefinic species were observed by in situ CIR–FTIR, as shown in Fig. 3. The intensities of the bands in the region of 1800–1600 cm⁻¹ and 1600–1500 cm⁻¹ were much higher as compared to those observed under 60 bar *n*-pentane pressure. This suggests that the higher supercritical pressure helped to reduce the formation of the surface coke precursors in supercritical *n*-pentane cracking on H-ZSM-5. Similar to that observed under 60 bar pressure, the bands assigned to aromatic and olefinic species were stable after their initial appearance, suggesting that the catalyst surface species reached a steady state rather quickly and did not change much for the rest of the time. The GC results were consistent with the FTIR analysis.

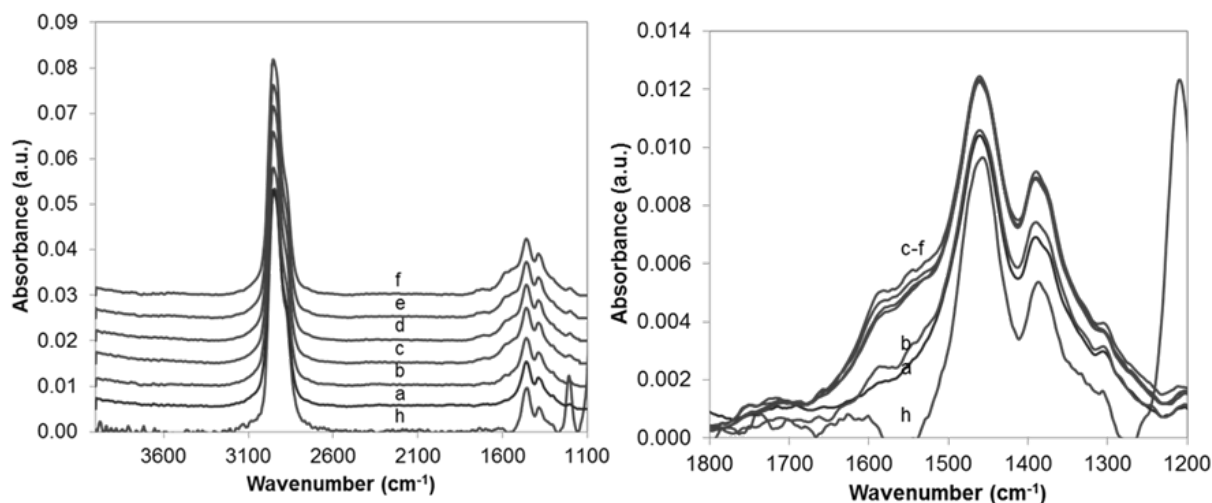


Fig. 1: In situ CIR–FTIR spectra of *n*-pentane flowing in annular reactor cell at 450 °C and 60 bar in the presence of H-ZSM-5 (Si/Al=11.5) catalyst, 9.5 ml/min *n*-pentane after a time on stream of : a) 1 min; b) 7 min; c) 39 min; d) 80 min; e) 110 min; f) 135 min; h) blank experiment spectra at 35 min, (left) overall spectra and (right) spectra region between 1800 to 1100 cm⁻¹.

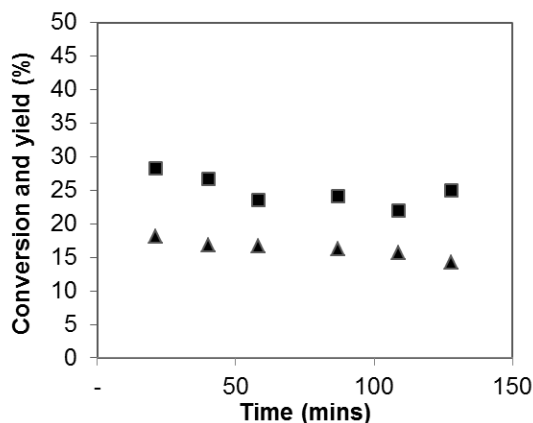


Fig. 2. *n*-Pentane conversion (■) and C₁-C₅ product yield (▲) on H-ZSM-5 (Si/Al=11.5), at 60 bar, 450 °C, under 9.5 ml/min *n*-pentane flow.

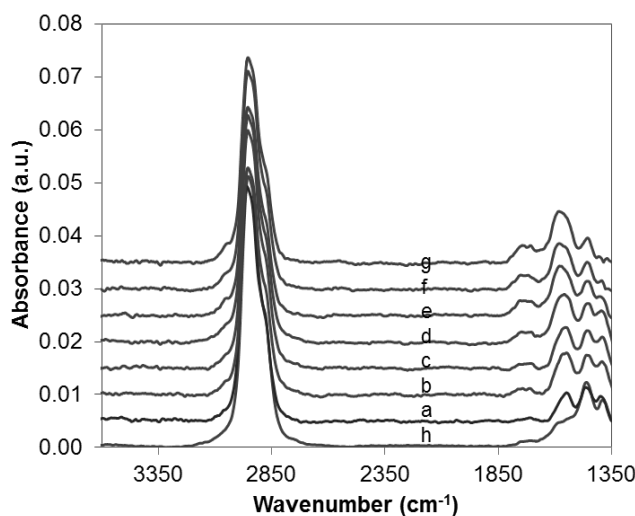


Fig. 3. In situ CIR-FTIR spectra of *n*-pentane flowing in the annular reactor cell at the 450 °C and 34 bar supercritical conditions in the presence of H-ZSM-5 (Si/Al=11.5) catalyst. Time on stream with a 7.8 ml/min *n*-pentane inlet flow: a) 1 min; b) 23 min; c) 31 min; d) 85 min; followed by 5 ml/min *n*-pentane inlet flow: e) 225 min; f) 248 min; g) 286 min. For comparison, spectra h at 60 bar, for a 9.5 ml/min *n*-pentane flow with a time on stream of 110 min.

The H-ZSM-5 catalyst had a much better activity than the zeolite Beta. Table 3 compares the performance of these two catalysts based on GC results. The average *n*-pentane conversion on the H-ZSM-5 was almost twice of that on the zeolite Beta under same supercritical conditions. On the other hand, the zeolite Beta had a higher amount of olefinic and aromatic surface species, in the FTIR spectral regions of 1650–1550 cm⁻¹ and 2000–1665 cm⁻¹, as shown in Fig. 4. The zeolite Beta decayed at a fast rate, with the *n*-pentane conversion decreasing from 18% to 8% in 2 h. The TPO results confirmed higher coke formation on the zeolite Beta. The used zeolite Beta sample had a broader oxidation peak than the used H-ZSM-5 sample with the peak temperature shifting to higher temperatures, indicating that the coke formed on

zeolite Beta had a lower H/C ratio, i.e., more highly reacted aromatic or olefinic in nature. The measured coke amounts per *n*-pentane feed on H-ZSM-5 and zeolite Beta were 0.12 mg C/g fuel and 0.14 mg C/g fuel, respectively.

The higher coking rate and faster decay of zeolite Beta is consistent with literature findings [3,4] and can be explained by the pore structure of zeolite Beta. The large Beta pores and supercages combined with high acidity, enhanced the formation of aromatic and olefinic coke precursor species, by hydrogen transfer reaction and resulted in a rapid deactivation of the catalyst [4]. On the other hand, the smaller pore channel of the H-ZSM-5 did not favor the formation of coke. The results from this study indicated that the pore structure plays an important role in the formation of catalyst surface intermediates/products and thus affected the catalyst activity and stability in supercritical *n*-pentane cracking.

No significant differences in product distributions were observed over both zeolites, which were dominated by alkane products. Both catalysts had a high selectivity to propane, ethane, ethylene, and isopentane. The yield to ethylene and propylene was low. The paraffin/olefin (P/O) ratio was much higher than 1 on both catalysts under the supercritical conditions tested. The higher P/O ratio indicated that bimolecular cracking mechanisms were significantly favored under the supercritical conditions for *n*-pentane cracking.

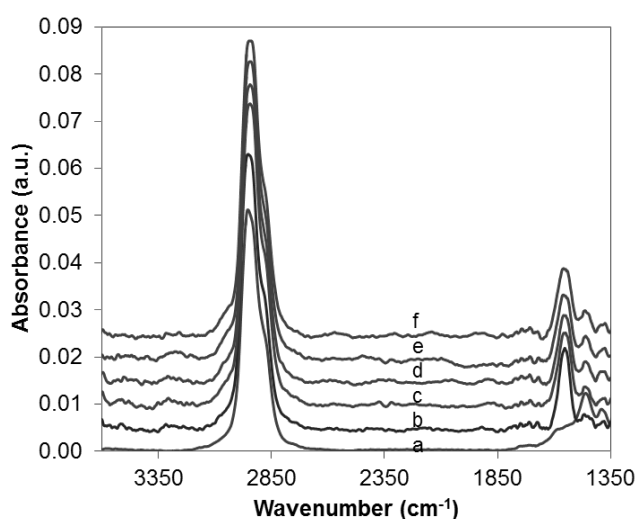


Fig. 4. In situ CIR-FTIR spectra of *n*-pentane flowing in an annular reactor cell at 450 °C and 60 bar in the presence of zeolite Beta (Si/Al=12.5), with 9.5 ml/min *n*-pentane inlet flow after time on stream: b) 1 min; c) 28 min; d) 48 min; e) 68 min; f) 103 min. For comparison: a) spectra of *n*-pentane over H-ZSM-5 at 60 bar, 450 °C, with 9.5 ml/min *n*-pentane flow after 110 min time on stream.

Table 3. Results of *n*-pentane cracking over H-ZSM-5 (Si/Al=11.5) in the CIR–FTIR reactor.

Catalyst	T (°C)	P (bar)	<i>n</i> -pentane flow (ml/min)	Residence time (s)	Y-P _(C₁-C₅) ^a (%)	Y-O _(C₁-C₅) ^b (%)	X-C ₅ ^c (%)
H-ZSM-5	450	60	9.5	1.0	13.3	3.0	24.9
Beta	450	60	9.5	1.0	2.9	0.8	11.2

- Average yield to C₁–C₅ paraffin
- Average yield to C₁–C₅ olefins
- Average *n*-pentane conversion

1.2 Bi-functional Pt-H-ZSM-5 catalyst

A Pt-modified H-ZSM-5 catalyst was evaluated for the promotion of dehydrogenation activity for higher olefin selectivity, while maintaining high cracking activity by the intrinsic H-ZSM-5 Brønsted acidity. The 1.5wt%Pt/H-ZSM-5 catalyst was prepared by ion-exchange. Fig. 5 shows the IPA TPD–MS profile on both the H-ZSM-5 and Pt/H-ZSM-5 catalysts with a Si/Al=11.5. The evolution of the mass 42, 41 and 39 peaks close to 300 °C, as observed on both H-ZSM-5 and 1.5wt%Pt/H-ZSM-5, was due to the formation of propylene by IPA decomposition on the Brønsted acid sites. The additional higher temperature peak, at ~360 °C, observed in TPD–MS profile of 1.5wt%Pt/H-ZSM-5, was attributed to the decomposition of IPA in the presence of Pt. The estimated Brønsted acid site densities on H-ZSM-5 and 1.5wt%Pt/H-ZSM-5 were 418 μmol/g and 191 μmol/g, respectively. The estimated metal site density based on the high temperature peak area was ~72 μmol/g. This was close to the amount of Pt on the catalyst, which is 77 μmol/g. This suggests that the Pt was well dispersed within the H-ZSM-5 matrix. This was consistent with the 62% Pt dispersion measured by H₂ chemisorption.

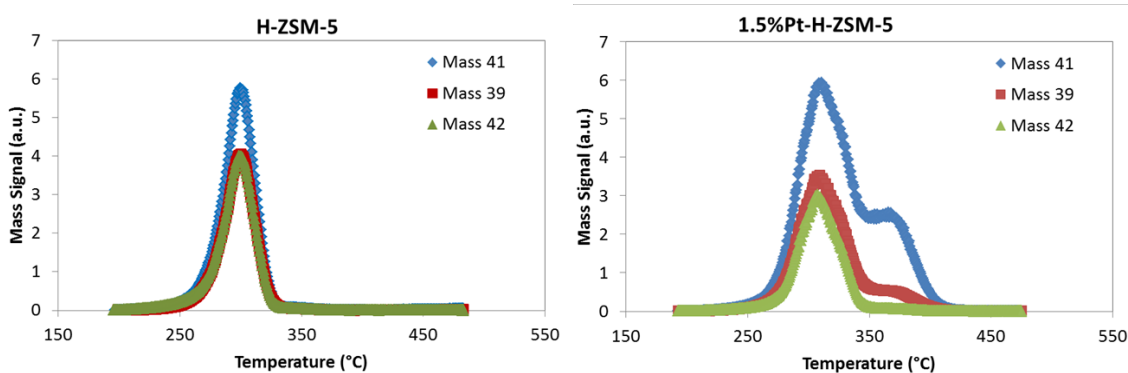


Fig. 5. Temperature programmed desorption–mass spectrometry of isopropylamine over (left) H-ZSM-5 (Si/Al=11.5) and (right) 1.5wt% Pt/H-ZSM-5.

The incorporation of Pt improved the olefin selectivity of H-ZSM-5-catalyzed supercritical *n*-pentane conversion. Fig. 6 compares the product distribution from *n*-pentane cracking on the H-ZSM-5 and 1.5 wt%Pt/H-ZSM-5 catalysts. The formation of pentene, C₅H₁₀, on the

1.5wt%Pt/H-ZSM-5, which was negligible on the H-ZSM-5, was due to the dehydrogenation activity of Pt. The formation of ethylene and propylene also increased on the 1.5wt%Pt/H-ZSM-5 catalyst. The selectivity to C₁–C₅ olefins increased from 16% on H-ZSM-5 to 21% on 1.5wt%Pt/H-ZSM-5. On the other hand, the total yield of C₁–C₅ products decreased from 57% on H-ZSM-5 to 37% on 1.5wt%Pt/H-ZSM-5, due to the lowering of the Brønsted acid site density by Pt exchange.

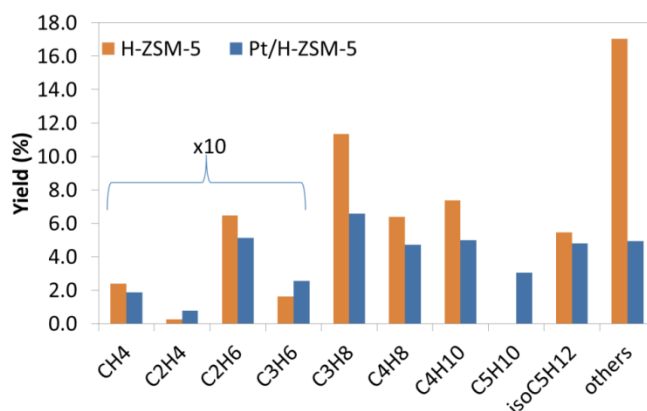


Fig. 6. Product yield of *n*-pentane cracking on H-ZSM-5 and 1.5wt%Pt/H-ZSM-5 (both Si/Al=11.5) at 34 bar, 450 °C after a time on stream of 30 min. The residence times were $\tau=1.5$ s for ZSM-5 and $\tau=1.0$ s for 1.5wt%Pt/H-ZSM-5.

The 1.5wt%Pt/H-ZSM-5 (Si/Al=11.5) catalyst was also evaluated for supercritical *n*-heptane cracking. The objective was to compare catalyst activity and durability with that of *n*-pentane cracking under supercritical conditions to evaluate the effect of fuel. An additional examination was conducted on the 1.5 wt%Pt/H-ZSM-5 performance under subcritical *n*-heptane conditions to understand the benefit of supercritical cracking. The subcritical testing condition was set at 22 bar ($P_r=0.8$) and 450 °C ($T_r=1.338$), and the supercritical testing condition was at 41 bar ($P_r=1.5$) and 450 °C ($T_r=1.338$). The volumetric residence time for both conditions was about 1 s, assuming 60% bed porosity with packed zeolite catalyst.

Under *n*-heptane at 41 bar and 450 °C, the 1.5wt%Pt/H-ZSM-5 catalyst had a much higher initial cracking activity, as well as olefin formation than the H-ZSM-5 catalyst, as shown in Fig. 7. The total C₁–C₅ and olefin C₁–C₅ yields at 30 min were 34.8% and 10.9%, respectively, on 1.5wt%Pt/H-ZSM-5. On the other hand, the total C₁–C₅ and olefin C₁–C₅ yields were 22.1% and 7.3% on H-ZSM-5, respectively. However, the selectivity to C₁–C₅ olefins was not significantly different on both of these two catalysts. Both catalysts decayed during the 2 h testing time and reached similar activity at the end of run, as shown in Fig. 8. The Pt sites may have sintered or decayed due to coke formation and had a decreasing contribution to catalyst activity with time. The FTIR spectra during reaction did not show obvious differences between the H-ZSM-5 and 1.5wt%Pt/H-ZSM-5 catalysts, indicating similar catalyst surface species during reaction.

The estimated coke deposition from *n*-heptane cracking was similar on both used samples, about 12 g coke per g catalyst. This is consistent with the FTIR findings, where no obvious

differences were observed. The decay rates of both the 1.5wt%Pt/H-ZSM-5 and H-ZSM-5 catalysts were higher in *n*-heptane than in *n*-pentane. This was probably due to a higher cracking rate of *n*-heptane on these catalysts as compared to that of *n*-pentane, as well as the lack of hydrocarbon densification in ZSM-5 pores as indicated by FTIR spectra.

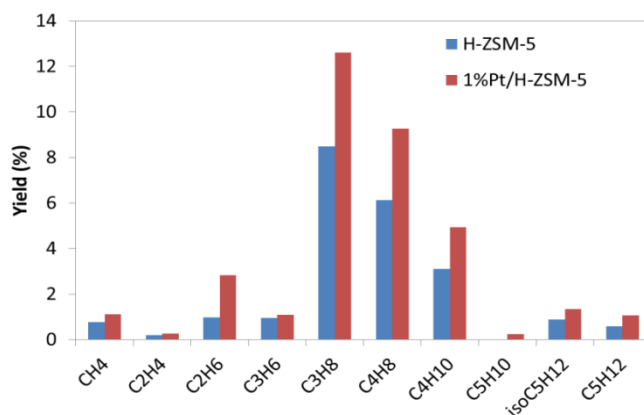


Fig. 7. Catalytic cracking of *n*-heptane on H-ZSM-5 and 1.5wt%Pt/H-ZSM-5 (both Si/Al=11.5) under 450 °C and 41 bar supercritical conditions after a time on stream of 30 min.

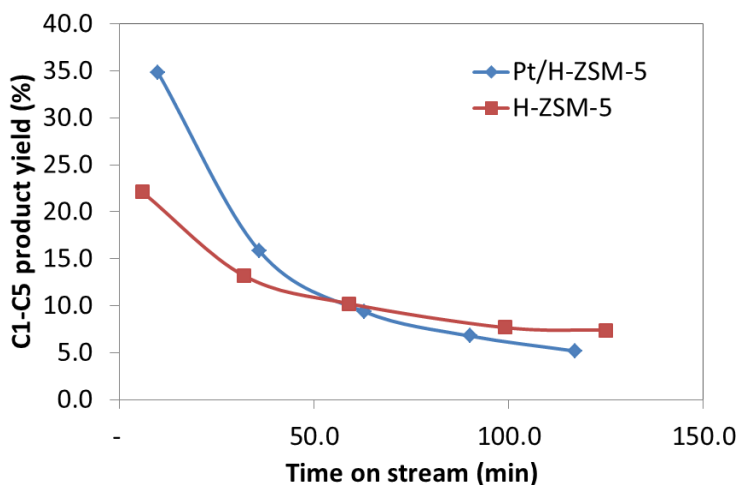


Fig. 8. Catalytic cracking of *n*-heptane on H-ZSM-5 and 1.5wt%Pt/H-ZSM-5 (both Si/Al=11.5) under 450 °C and 41 bar supercritical conditions.

Fig. 9 compares the yield to C₁–C₅ products and C₁–C₅ olefins on 1.5 wt%Pt/H-ZSM-5 at 41 and 22 bar *n*-heptane. The catalyst had much higher cracking activity as well as olefin formation at 41 bar, than at 22 bar. The FTIR spectra also showed that more olefin and aromatic formation occurred on the catalyst at 22 bar, as shown in Fig. 10. The estimated area under the C–H stretch band, in the region of 2700 to 3100 cm⁻¹, and for the olefinic and aromatic C–C stretch bands in the region of 1600 to 1300 cm⁻¹, are listed in Table 4. The C–H stretch band was mostly due to the presence of *n*-heptane and its intensity increased with the operating pressure, therefore resulted in an increased area at 41 bar. However, the area under the bands at 1600 to 1300 cm⁻¹ was similar for both pressures, indicating relatively higher amount of olefins and aromatics at 22 bar *n*-heptane.

The samples used under the supercritical and subcritical *n*-heptane conditions exhibited similar weight changes (~12 wt%) during TPO analyses, as shown in Fig. 11, indicating a similar total amount of coke formation on the catalyst. However, the amount of coke per g of *n*-heptane fed to the reactor was much lower at 41 bar, due to a much higher *n*-heptane flow. Both runs at 41 bar and 22 bar *n*-heptane, were kept at same volumetric residence time of 1 s. The coke per heptane fed was 0.14 g/g *n*-heptane at 41 bar and 0.25 g/g *n*-heptane at 22 bar. Both samples exhibited a broad TPO peak over the temperature range of 400 to 475 °C, while the sample tested at 22 bar showed additional peaks at temperatures higher than 500 °C. This indicated that more graphitic or hard coke was formed on catalyst under subcritical *n*-heptane conditions, thus caused a lower catalytic activity. The results also suggested that the supercritical *n*-heptane conditions helped to minimize coke formation due to the in situ extraction of coke or coke precursors by the supercritical fluid.

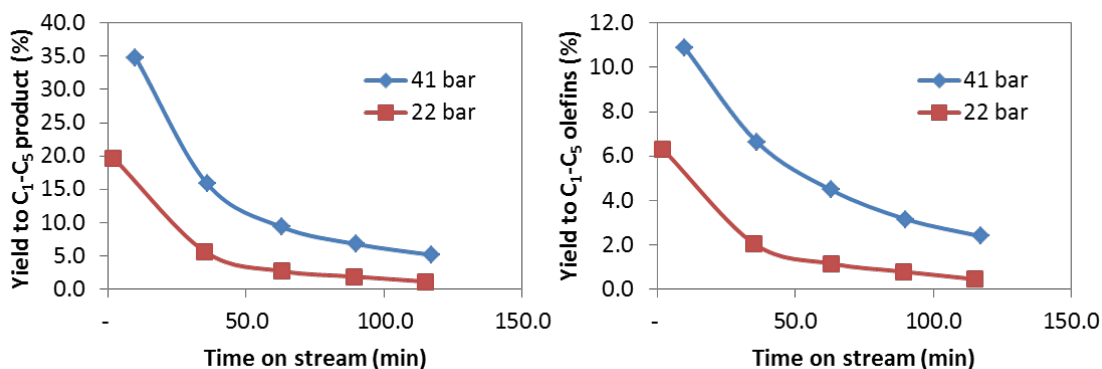


Fig. 9. The effect of pressure on catalytic cracking of *n*-heptane on 1.5wt%Pt/H-ZSM-5 at 450 °C: (left) yield to C₁-C₅ products and (right) yield to C₁-C₅ olefins.

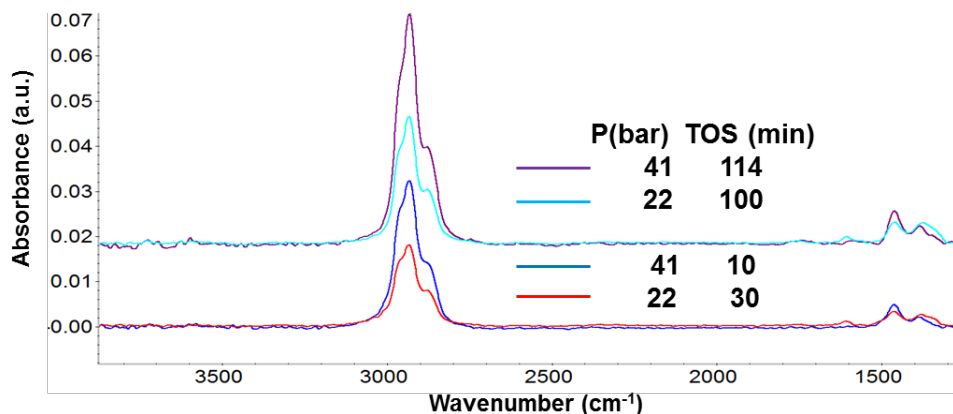


Fig. 10. In situ FTIR spectra of *n*-heptane cracking on 1.5wt%Pt/H-ZSM-5 with time on stream under 41 bar supercritical and 22 bar subcritical *n*-heptane pressures, respectively, with both at 450 °C.

Table 4. Estimated area under FTIR bands for *n*-heptane cracking on 1.5wt%Pt/H-ZSM-5 at 450 °C.

P (bar)	2750–3100 cm ⁻¹ (C–H stretch)	1300–1600 cm ⁻¹ (C=C & aromatic C–C stretch)
41	5.01	0.75
22	2.64	0.80

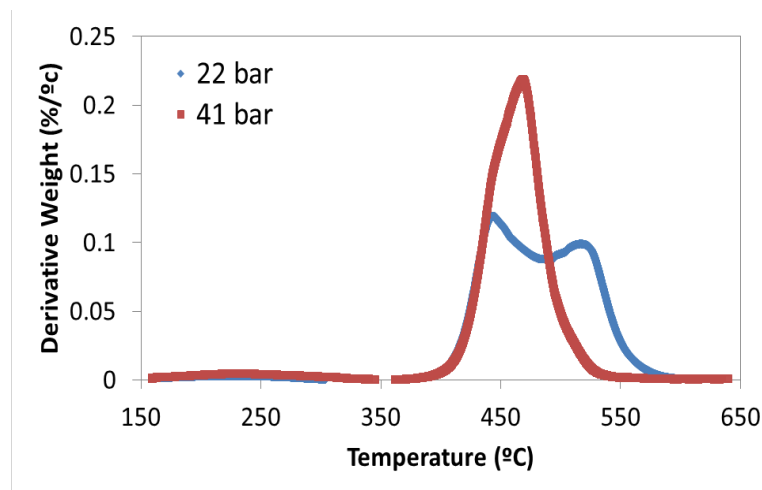


Fig. 11. Temperature programmed oxidation of used samples for *n*-heptane cracking at 41 bar supercritical and 22 bar subcritical *n*-heptane pressures, respectively, with both at 450 °C.

1.3 Multi-functional Pt-H-ZSM-5 catalyst

Cs exchange was examined in the 1.5wt%Pt/H-ZSM-5 (Si/Al=11.5) catalyst in an effort to reduce the amount of Brønsted acid sites and to improve the stability of catalytic activity during supercritical *n*-heptane cracking. The results showed that the exchange of 25% and 50% Cs, to form the 1.5wt%Pt/Cs_{0.25}+H_{0.75}-ZSM-5 and 1.5wt%Pt/Cs_{0.5}+H_{0.5}-ZSM-5 compositions, did not result in improved catalyst durability. The measured total coke deposits on the Cs-exchanged catalysts were measured to be about 12wt% by TPO, which was the same as that on the 1.5wt%Pt/H-ZSM-5 and H-ZSM-5 samples (also both Si/Al=11.5). No effect of the exchanged Cs on the oxidation behavior of the deposited coke was observed. In addition, all the samples tested for *n*-heptane cracking for a total of 2 h time on stream lost most of the surface area and pore volume due to coke formation, indicating pore closure during reaction.

2.0 Atomic Modeling

2.1 Atomic Model Basis – Zeolite Interactions with Supercritical *n*-Pentane

The combined observations of atomic modeling and CIR–FTIR investigations did not produce evidence of supercritical low molecular weight hydrocarbon densification inside the H-ZSM-5 framework, which was previously observed for *n*-heptane in Y zeolite [5]. The equilibrium supercritical pentane adsorption in ZSM-5 was predicted with GCMC simulations using TraPPE forcefields [6]. A constant particle number–isobaric–isothermal (NPT) ensemble was used to determine *n*-pentane chemical potential under the 450 °C and 60 bar supercritical conditions. This *n*-pentane chemical potential was then equilibrated with the internal accessible volume in a 2×2×4 ZSM-5 supercell. The calculated equilibrium loading was 0.6 *n*-pentane molecules per ZSM-5 unit cell, which was equivalent to a loading of 0.03 g/cm³, if the internal accessible volume is taken to be equivalent to the 2058 Å³ internal van der Waals surface per ZSM-5 unit cell. The ZSM-5 supercell model equilibrated with supercritical pentane is shown in Fig. 12. This pentane adsorption level is close to the supercritical density of pentane ($\rho=0.08$ g/cm³), and can be interpreted to indicate that the opportunity for pentane molecules to be potentially influenced by one another and their cracking products is significantly reduced within the ZSM-5 framework. This result was used to support the model basis of 1 pentane molecule per unit cell under supercritical conditions. Force fields are not presently available to describe local hydrocarbon physisorption interactions at Al-substituted protonated acid sites within zeolites.

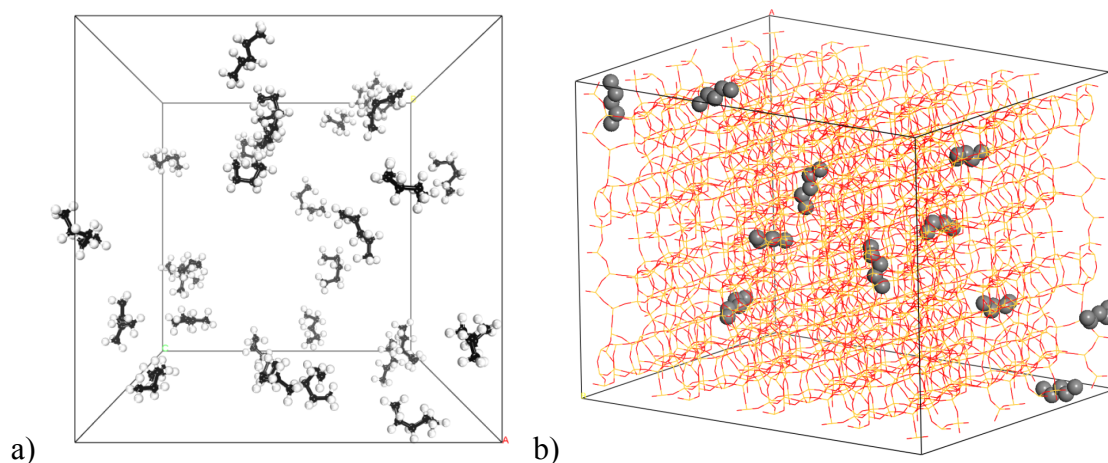


Fig. 12. Atomic models for supercritical *n*-pentane predictions at 450 °C and 60 bar: a) perspective view supercritical *n*-pentane phase (0.08 g/cm³) with carbon atoms in black and hydrogen atoms in white, and b) oblique view of predicted equilibrium supercritical *n*-pentane adsorption in ZSM-5 zeolite 2x2x4 supercell, where oxygen atoms are shown as red lines, silicon atoms as yellow lines, and united carbon atoms as gray balls.

2.1.1 Influence of Zeolite Si/Al Ratio and Al Distribution on Lattice and Brønsted Acid Site Characteristics

The survey first investigated Al substituted H-ZSM-5 candidate host structures. Full VASP minimizations of both lattice parameters and atomic positions were made using projector augmented wave potentials with the generalized gradient exchange–correlation approximation of Perdew, Burke, and Ernzerhof (PAW/GGA-PBE) [7] and the Grimme DFT-D2 [8] dispersion potentials for van der Waals contributions. This paragraph summarizes the findings

were reported in a recent publication [9]. The model configurations, detailed in Table 5, examined three different Si/Al ratios (inversely proportional to Al density) with Al uniformly distributed with the highest possible symmetry, in order to minimize the number of symmetry-equivalent Al substitution sites (T-sites) investigated. As shown in Table 5, two of the Si/Al ratios corresponded to the commercial zeolites investigated experimentally. Another model configuration probed the Al distribution as next-next nearest-neighbor pairs for the lowest Si/Al ratio of 11. The optimized models showed that increases in the density of uniformly substituted Al was manifested in an increased lattice volume and Brønsted acid site O–H bond distance, and a decreased the polarization of both the lattice and Brønsted acid sites (decreased proton charge). These changes were attributed to the increased lattice stability and covalency with increasing Al density, predicted by the electronic density of states (DOS), as shown in Fig. 13. The increase in Al proximity in the paired configurations further increased the lattice volume, and increased the polarization (ionicity) of both the lattice and Brønsted acid sites (increased proton charge).

Table 5. Corresponding atomic model and experimental (H)-ZSM-5 compositions with varying Al substitution selected for investigation.

Atomic Models				Experiment	
Model Si /Al	Unit Cell Composition	Al T-site substitution (<i>distribution</i>)	Adjacent Protonated O Site	Zeolyst Int. Product No.	Si/Al
11.0	Si ₈₈ Al ₈ O ₁₉₂ H ₈	a- T6 (<i>paired</i>) b- T12, T6 (<i>uniform</i>)	a- O18 b- O18,O20	CBV 2314	11.5
15.0	-	-	-	CBV 3024E	15.0
23.0	Si ₉₂ Al ₄ O ₁₉₂ H ₄	T12 (<i>uniform</i>)	O20	CBV 5524G	25.0
95.0	Si ₉₅ AlO ₁₉₂ H	T12	O20	-	-
~ ∞	Si ₉₆ O ₁₉₂	-	-	-	-

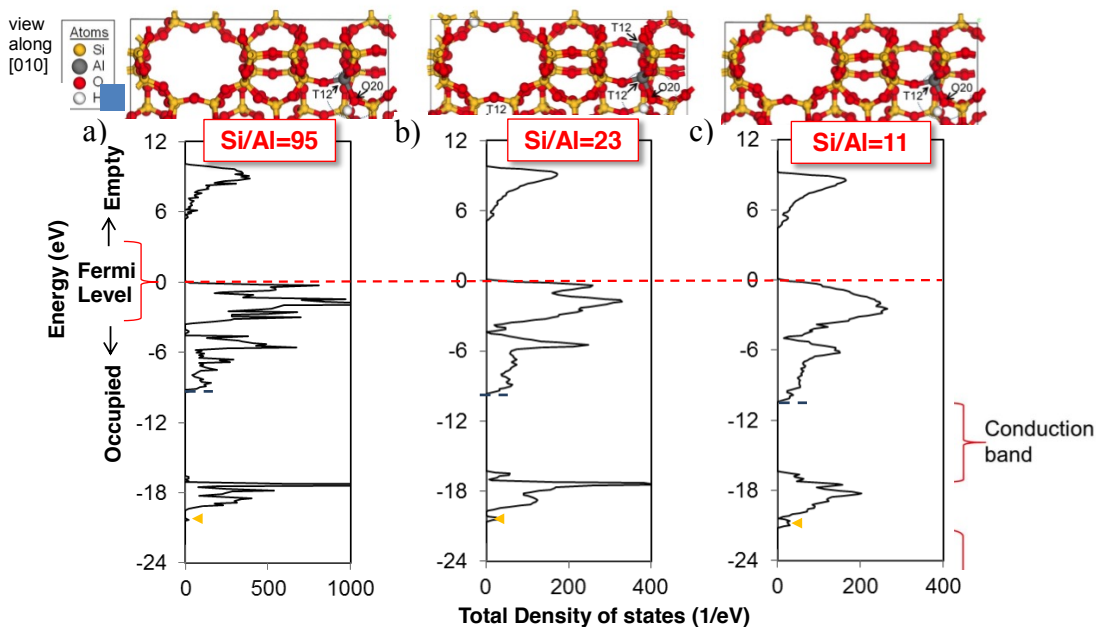


Fig. 13. Fully VASP minimized atomic models (top) and corresponding electronic density of states (bottom) of H-ZSM-5 with Al uniformly distributed in T12 and T6 Brønsted acid sites with Si/Al ratios of a) 95, b) 23, and c) 11. The results were adapted from reference [9].

2.1.2 Influence of Zeolite Si/Al Ratio and Al Distribution on Brønsted Acid Site Adsorption Reactions

Atomic modeling investigations of the H-ZSM-5 Brønsted acid site reactivity with varying Si/Al ratio and Al distribution found correlations in the predicted varying lattice and Brønsted acid site characteristics with the strength of the interactions with the IPA and *n*-pentane representative probe molecules. The VASP minimizations of ionic positions were conducted on a single probe molecule interacting with selected Brønsted acid sites in the fully-minimized H-ZSM-5 lattices. The ground state electronic enthalpies for the adsorption interactions with H-ZSM-5 of varying Si/Al ratio are shown in Fig. 14 (sign convention: negative ΔH_{ads} values are exothermic and favorable). This paragraph summarizes the findings detailed in a recent publication [9]. The strength of the spontaneous protonation of IPA on Brønsted acid sites increased with Al density, stabilized by the increased electron density transferred with increasing lattice covalency. Corresponding TPD–MS measurements showed that the H-ZSM-5 IPA cracking reactivity increased with Al density. The strongest IPA adsorption was measured at the T12 Brønsted site in the uniform Si/Al=11 configuration. These predictions are consistent with the increased IPA peak desorption temperature and peak area measured by TPD–MS, which could be interpreted to indicate an increase in the strength of the reacting Brønsted acid sites with decreasing Si/Al ratio. The IPA adsorption also increased with Al proximity, due to the improved stabilization of the protonated IPA intermediate by the more ionic lattice. Here, the lattice deprotonation energy, which decreased with increasing Al

density and increasing Al proximity, had a stronger influence of the IPA adsorption reaction. The exothermic *n*-pentane physisorption strength also increased with Al density, due to the increased van der Waals interactions with the increasingly covalent lattices. However, the endothermic *n*-pentane backbone protonation to form a *n*-pentyl carbonium was stabilized by the improved charge redistribution in the more ionic lattices formed at lower Al densities or increasing Al proximity. Here, the *n*-pentyl carbonium stabilization interaction with the deprotonated lattice was predicted to have a predominating influence on the pentane protonation reaction.

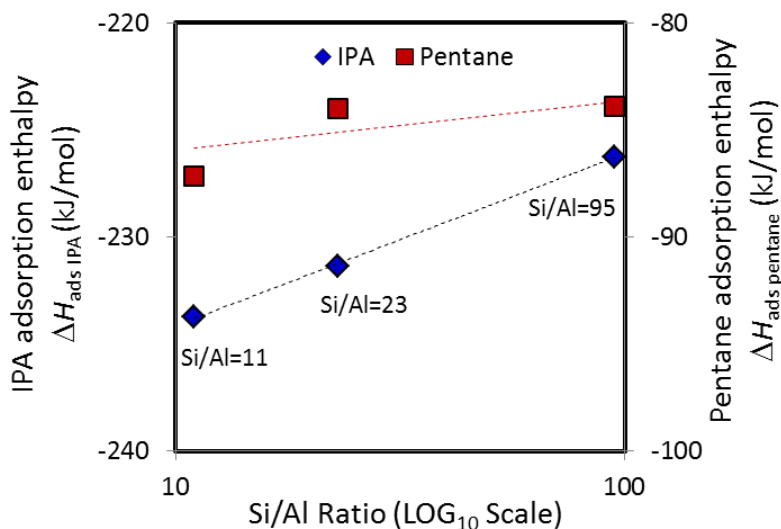


Fig. 14. The predicted correlation of the isopropylamine (IPA) chemisorption with spontaneous protonation and *n*-pentane physisorption ground state electronic reaction enthalpies at T12 Brønsted acid sites in H-ZSM-5 with varying Si/Al ratios and with uniform Al distribution.

2.1.3 Influence of Zeolite Si/Al Ratio and Al Distribution on Brønsted Acid Site *n*-Pentane Conversion Reactions

VASP ionic minimizations were completed for a matrix of the key intermediates for four major reaction stages for *n*-pentane cracking and coke precursor formation at the Brønsted acid sites in H-ZSM-5 structures with varying acid site characteristics, including: 1) protonation, followed by pentyl carbonium (pentonium) cracking, 2) pentane–propyl carbenium (propenium) hydride transfer, 3) pentyl carbenium (pentenium) isomerization, and 4) propenium–propylene coupling (oligomerization). The cumulative ground state electronic reaction enthalpies are plotted in Fig. 15 for the matrix of reaction intermediates, where the last propenium–propylene coupling reaction was determined using the sum of the reactions producing the propenium complex and releasing propylene for the reactant energies. There are subtle, but consistent trends of decreasing physisorption, decreasing protonation, and increasing cracking reaction enthalpies with increasing original Brønsted proton charge (or conversely with increasing original Brønsted O–H bond length). The most significant differences in reaction enthalpies were predicted for the less desirable hydride transfer and

coupling mechanisms facilitated by the increasing lattice ionicity with increasing Al density (Si/Al=23, uniform Al configuration) or increasing Al proximity (Si/Al=11, paired Al configuration).

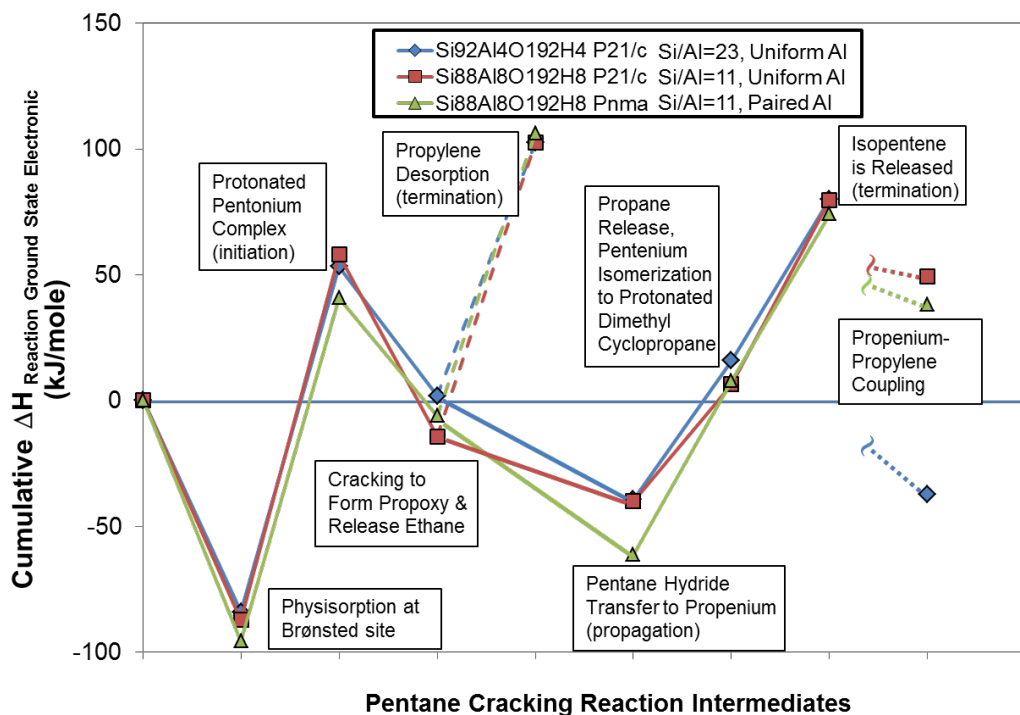


Fig. 15. VASP atomic modeling reaction enthalpy predictions for *n*-pentane cracking and bimolecular reactions in H-ZSM-5 with varying Si/Al ratios and Al distributions.

2.2 Extrinsic Zeolite Functionality

2.2.1 Modes of Incorporating Atomic Pt Sites

Atomic modeling was used to investigate the stability, configuration, charge distribution, and reactivity of atomic Pt extrinsic “single-sites” that could be incorporated within H-ZSM-5 pore networks with different synthetic approaches. Atomic modeling showed that the $\text{Pt}(\text{NH}_3)_4^{+2}$ precursor complex can be accommodated within the H-ZSM-5 pore channels. The atomic models were configured with lowest feasible loading of 1 Pt atom per H-ZSM-5 unit cell, which corresponded to 3.3 wt% Pt and is the closest possible stoichiometry to the 1.5wt% Pt incorporated experimentally. These atomic Pt sites represent ideal scenarios for the highest possible Pt utilization and dispersion that are challenging to investigate experimentally, including the 3 configurations illustrated in Fig. 16: a) “exchanged Pt” from the ion-exchange of a Pt precursor in NH_4^+ -ZSM-5, followed by calcination, b) “reduced Pt” from the impregnation or exchange, calcination, and reduction of a Pt precursor at a Brønsted acid site, and c) “inter-ring Pt” from Pt precursor chemical vapor deposition, followed by calcination. The enthalpy of Pt adsorption, $\Delta H_{\text{ads Pt}}$, was determined referencing a spin-

polarized atomic Pt and the H-ZSM-5 lattice structures. The modeling showed that the mode of atomic Pt incorporation had a more significant influence on the Pt site properties than the characteristics of the H-ZSM-5 lattice. The Pt adsorption strength, in terms of $\Delta H_{\text{ads Pt}}$, varied over a wide range with the Pt incorporation mode, but not with the Si/Al ratio. For all reduced and exchanged configurations, the substitution of Pt for one Brønsted acid site proton was always more favorable than for two Brønsted acid site protons. The inter-ring Pt configurations were the most stable and the reduced Pt configurations were the least stable. The incorporated Pt atoms were positively charged, where the Pt charges were the lowest for the most stable inter-ring Pt configurations. The total electronic DOS are also shown in Fig. 16 for the Pt/H-ZSM-5 with uniform Si/Al=11 with the three different Pt site configurations. This can be compared to the electronic DOS of H-ZSM-5 with uniform Si/Al=11 in Fig. 13c. The superimposed Pt d level partial DOS occur at the top of the valence band near the Fermi level (highest occupied electronic level). In the inter-ring Pt/H-ZSM-5 model, with Si/Al=11 and uniform Al, these levels are separate and nearly full, shifting the lattice electronic levels to lower energies. However, in the reduced Pt/H-ZSM-5, with Si/Al=11 and uniform Al, the Pt levels are partially full and overlap with the lattice electronic levels, without imparting significant lattice stabilization.

The relatively small H-ZSM-5 pore channels and intersections limit the size of the Pt clusters that can be accommodated. The models showed that octahedral 6 Pt atom is the largest cluster that could comfortably fit within an H-ZSM-5 pore intersection; however, this would block hydrocarbon diffusion. Ideally, a 2 or possibly 3 Pt atom cluster is the largest that can be accommodated while still providing facile reactant passage between bi-functional sites. The loading of a Pt dimer on H-ZSM-5 with Si/Al=11 and uniform Al nearly doubles the $\Delta H_{\text{ads Pt}}$ per Pt atom. Stronger Pt dimer–lattice interactions were observed, including an increase in lattice iconicity (basicity) relative to the H-ZSM-5 alone.

2.2.2 Atomic Pt Site Reactivity Trends

Pentane reaction intermediates were investigated in the atomic Pt/H-ZSM-5 configurations using VASP ionic minimization calculations in order to determine whether the bi-functional Pt/ Brønsted reaction selectivity could be modified by changing the H-ZSM-5 intrinsic characteristics and/or the mode of Pt incorporation. The pentane electronic ground state adsorption enthalpies, $\Delta H_{\text{ads pentane}}$, were determined for the pentane adsorption on Pt and also on a nearby T12 Brønsted acid site in the minimized atomic Pt/H-ZSM-5 configurations. The plot in Fig. 17a shows that the incorporated Pt atom reactivity in H-ZSM-5 with Si/Al=11 and uniform Al, in terms of $\Delta H_{\text{ads pentane}}$, was inversely correlated to the strength of the Pt bonding interactions with the H-ZSM-5 framework, $\Delta H_{\text{ads Pt}}$. Dissociative pentane chemisorption occurred spontaneously on the more reactive exchanged and reduced atomic Pt configurations. The pentane adsorption in these two configurations was significantly stronger than on the nearby T12 Brønsted acid sites. Pentane did not adsorb on the most stable inter-ring Pt configuration, but rather migrated to physisorb between the Pt and a nearby Brønsted site. Here, the uniformly distributed Brønsted sites are in fairly close proximity ($< 7 \text{ \AA}$ apart) and interacted more strongly with pentane than the inter-ring Pt. So depending on the Pt configuration, it was predicted that atomic Pt either adsorbed pentane too strongly for facile desorption, or, was not competitive with the Brønsted sites. The mode of Pt incorporation

influenced the balance of the pentane intrinsic dehydrogenation enthalpy relative to the pentane adsorption. Fig. 17b shows that in all cases, pentane dehydrogenation on the atomic Pt sites was more favorable (less endothermic or more exothermic) compared to the moderately endothermic dehydrogenation on a nearby T12 Brønsted acid site. Pentane dehydrogenation on the exchanged Pt site was mildly endothermic, involving electron transfer to the covalently interacting pentene at the expense of increased lattice and Pt excess charges and accompanying polarization. Pentane dehydrogenation was moderately exothermic on the very reactive reduced Pt and also on the very stable inter-ring Pt, the latter due to strong backbonding electron-donating interactions with pentene double bond anti-bonding π^* orbitals. The pentane reaction on the exchanged Pt/H-ZSM-5 configuration offers the most favorable scenario, since the pentene dehydrogenation product could be more easily desorbed for turnover of the exchanged Pt catalytic site and to prevent further reactions leading to coke precursor formation. Numerous bi-functional reaction scenarios were evaluated for all of the atomic Pt/H-ZSM-5, showed that balanced bi-functional mechanisms could possibly be achieved on the inter-ring Pt/H-ZSM-5 configuration, where the possible sequence of events would be first Brønsted acid site cracking, followed by Pt dehydrogenation of the saturated products.

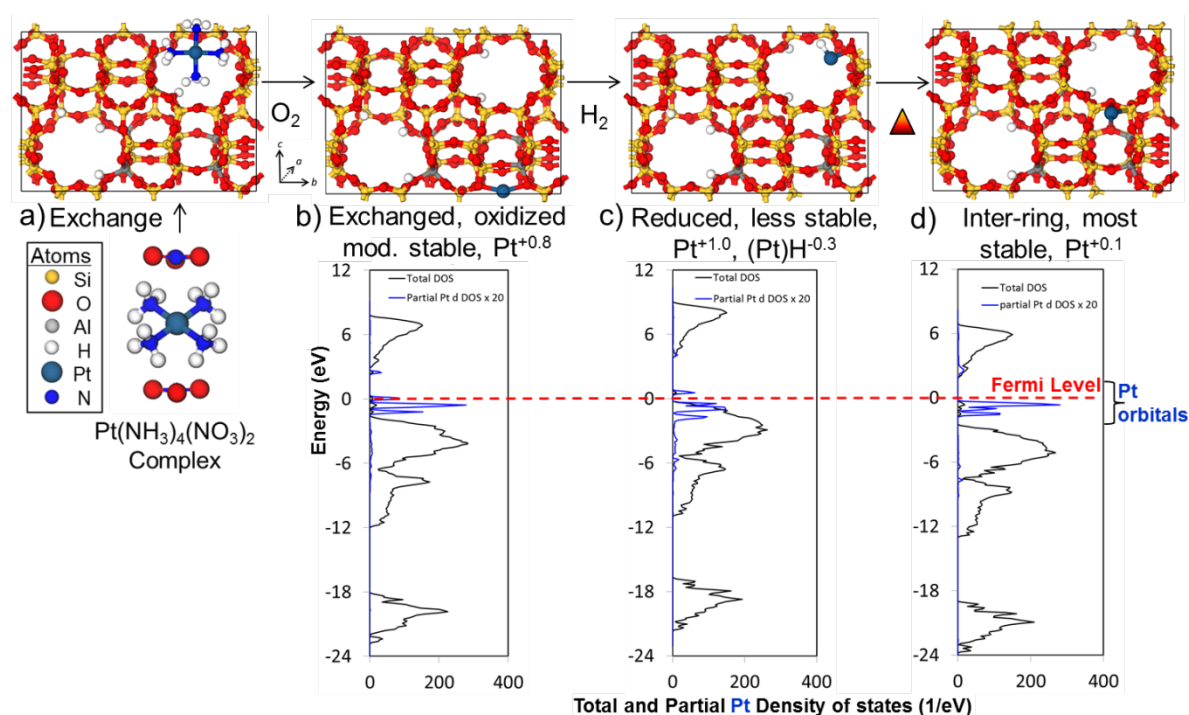


Fig. 16. VASP minimized atomic models (top) and corresponding electronic density of state predictions (bottom) of atomic Pt extrinsic sites incorporated with different synthetic modes in H-ZSM-5 with Si/Al=11 and uniformly distributed Al, including a) exchange of $\text{Pt}(\text{NH}_3)_4^{+2}(\text{NO}_3)_2$ precursor, b) atomic Pt exchanged and oxidized at T12 Brønsted site, c) atomic Pt exchanged and reduced at T12 Brønsted site, and d) inter-ring Pt impregnated into pore wall after calcination.

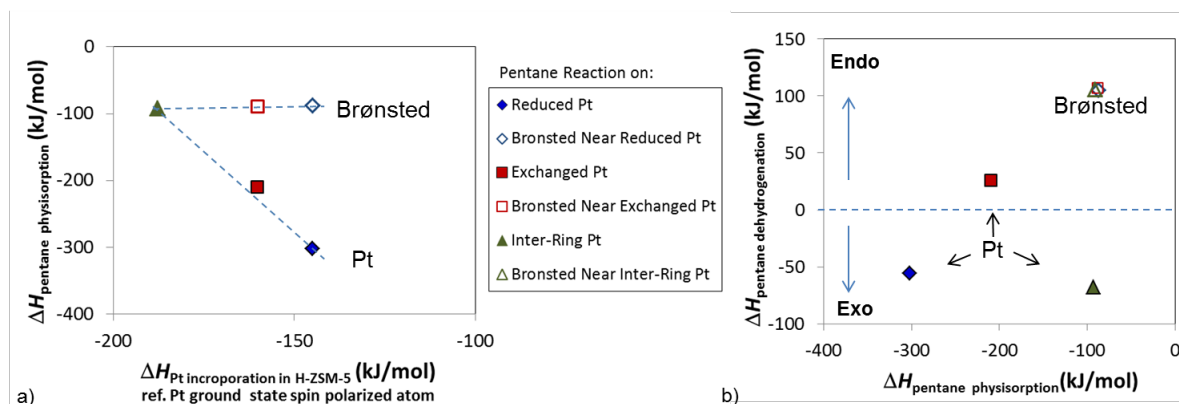


Fig. 17. Ground state electronic reaction enthalpies for pentane reactions with nearby atomic Pt and T12 Brønsted sites in H-ZSM-5 with Si/Al=11 and uniform Al with different atomic Pt incorporation modes: a) pentane physisorption versus Pt incorporation and b) intrinsic pentane dehydrogenation versus pentane physisorption.

2.3 Cs Alkali Modifier Functionality

2.3.1 Cs Incorporation Trends

Additional investigations were made to determine whether the exchange of Cs^+ for H^+ could modify the balance of bi-functional Pt/H-ZSM-5 hydrocarbon conversion mechanisms and stability with respect to coking. The rationale for multi-functional Pt/Cs+H-ZSM-5 included: a) Brønsted acid site titration to minimize undesirable cooperative hydride transfer and oligomerization mechanisms, b) alteration of the lattice/ Brønsted acid site ionicity/covalency to moderate bi-functional Pt/ H^+ reactivity, and c) the introduction of Cs^+ Lewis acid sites for possible new reaction mechanisms. Atomic modeling with the VASP code showed that up to 100% Cs^+ exchange could be accommodated in the H-ZSM-5 with Si/Al=11 and uniform Al, where Cs^+ is preferentially exchanged on stronger Brønsted acid sites at pore channel interactions. The electron donation from the electropositive Cs increased the Cs+H-ZSM-5 lattice and residual Brønsted acid site polarizations, which were maximized at 50% Cs^+ . The exchange of atomic Pt on residual T12 Brønsted acid sites remaining after Cs^+ exchange was predicted to decrease in favorability with increasing % Cs^+ , due to the inability of the lattice to accommodate excess electronic charge donated from Pt. The increased localization of the excess electronic charge is evident by comparing the electronic DOS shown in Fig. 18 for the exchanged atomic Pt/ $\text{Cs}_{0.25}\text{H}_{0.75}$ -ZSM-5 with Si/Al=11 and uniform Al configuration with those shown in Fig. 13c and Fig. 16b for the comparable configurations without Cs. The combined Cs and single-site exchanged Pt incorporation decreased the lattice polarization and moderated the polarization of the remaining Brønsted acid sites. These predictions guided the selection of Pt/Cs+H-ZSM-5, Si/Al=11.5 compositions with 25 and 50 atomic% exchanged Cs^+ for experimental evaluation.

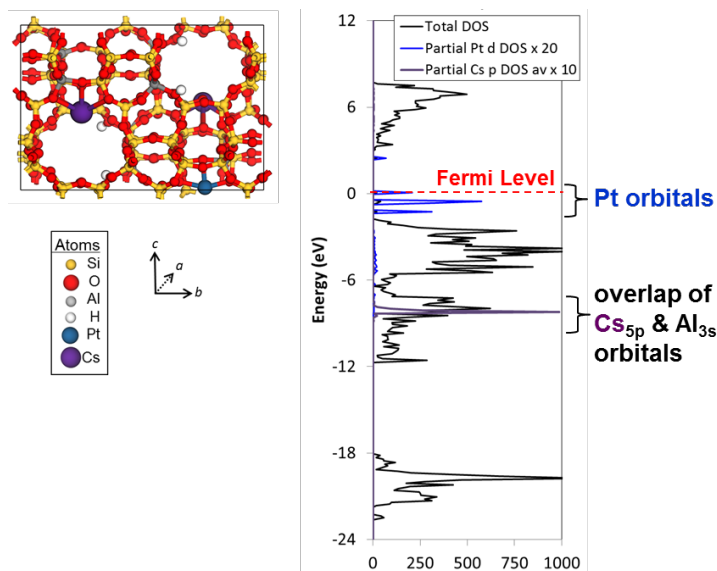


Fig. 18. Exchanged atomic Pt/Cs_{0.25}+H_{0.75}-ZSM-5 with Si/Al=11 and uniform Al configuration: (left) VASP minimized atomic model and (right) corresponding electronic density of state predictions.

2.3.2 Cs Modification of Bi-functional Reactivity

VASP ionic minimizations were conducted to investigate the impact of Cs incorporation on the Pt and Brønsted acid site reactivity in the H-ZSM-5 Si/Al=11 and uniform Al configuration. The atomic Pt and residual polarized Brønsted acid sites were more reactive with increasing % Cs exchange and more strongly adsorbed pentane (increased exotherms), as shown by the ground state electronic reaction enthalpies plotted in Figs. 19a and 19b. However, at the same time, increasingly less favorable reaction enthalpies (increased endotherms) were predicted for pentane dehydrogenation on either site with increasing Cs incorporation. This was due to the poor accommodation of excess electronic charge by the already electron-rich the Cs-modified lattice, required for stabilizing the dehydrogenation reactions. In addition, the Cs-destabilization of the exchanged atomic Pt hindered back-donation of excess electronic charge to the pentene product. The atomic modeling did not reveal evidence that the Cs⁺⋯O⁻ Lewis acid–Brønsted base strengths were sufficiently strong enough to directly contribute to coupled Lewis acid–Brønsted base dehydrogenation mechanisms.

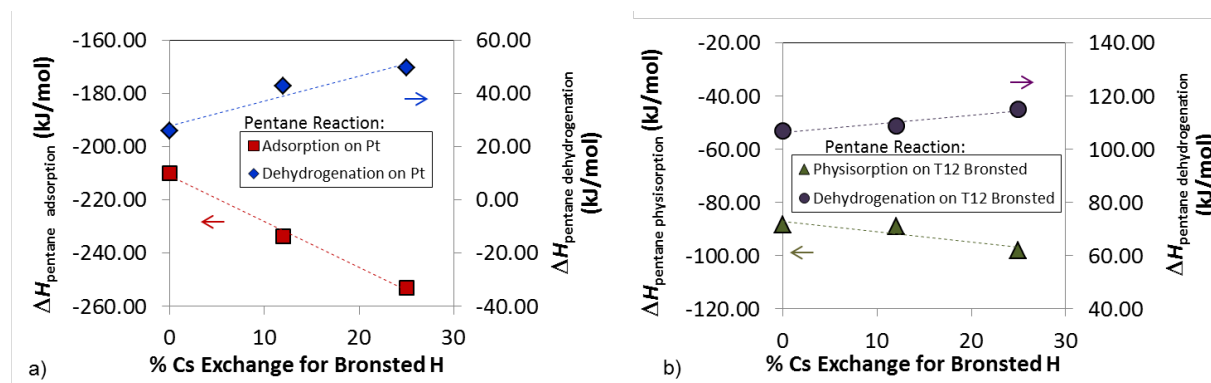


Fig. 19. Ground state electronic reaction enthalpies in exchanged atomic Pt/H-ZSM-5 with Si/Al=11 and uniform Al modified with varying % Cs exchange on T12 Brønsted sites for pentane adsorption and dehydrogenation reactions on: a) exchanged atomic Pt site and b) nearby residual T12 Brønsted acid site.

3.0 Heat Exchanger Rig Testing

Two catalyst candidates for endothermic hydrocarbon dehydrogenation were successfully tested in the UTRC Heat Exchanger rig under supercritical *n*-dodecane conditions (*n*-Dodecane is a surrogate fuel representative for the JP-7 and JP-8 jet fuels and has a critical temperature of 658 K and critical pressure of 1.8 MPa or 18 bar). The two catalyst candidates included 3wt% Pt / 0.6wt% Sn metal alloy catalyst loaded on Cabosil silica [from Professor Dumesic's group at the University of Wisconsin, part of the University of Utah (Utah) team and a 5.8wt% Mo/B-MFI catalyst with Si/B=70 [from Professor Lobo's group at UD, part of the Colorado School of Mines (CSM) team]. Each test involved suspending 1.1 wt% of the catalyst in *n*-dodecane by agitation in the fuel reservoir. A high precision fuel pump was used to feed the suspension at 4.6 ml/ml under 4.2 MPa (42 bar) pressure to a tubular heat exchanger reactor to achieve a residence time of 0.1 s (the reactor tube was made of Inconel 625 alloy and was coated internally with a SilcoKlean 1000 CVD amorphous silicon layer. The tube had dimensions of 0.07 cm ID, 0.32 cm OD, 60.96 cm length). The reactor was resistively heated by direct current. The power settings were progressively increased until tube blockage occurred, resulting in a significant increase in the pressure drop. The reactor heat sink was determined by subtracting the heat loss to the surroundings from the heat input at each temperature, where the heat loss was determined by separately calibrating each power setting in *n*-dodecane. A baseline run was conducted in neat *n*-dodecane under the same conditions that were used for the catalyst suspensions in *n*-dodecane.

The endotherms catalyzed in supercritical *n*-dodecane are plotted in Fig. 20 as a function of temperature, along with the pyrolysis endotherm of neat supercritical *n*-dodecane and the *n*-dodecane sensible heat capacity. Both catalyst endotherms were fairly similar in character. The catalyzed endotherms started to rise above the *n*-dodecane heat capacity at approximately 680–690 K, significantly lower in temperature (~100–110 K lower) compared to the onset of endothermic pyrolysis of the neat *n*-dodecane at approximately 790 K. In addition, the catalyst endotherm enhancement was found to be on the order of 310–350 J/g, compared to that of the pure *n*-dodecane at 800 K. The Utah team PtSn/Cabosil catalyst endotherm onset earlier in

temperature and was larger in value, however, the run was terminated earlier at 848 K. The CSM Mo/B-MFI catalyst did not plug until 925 K. The blockage in the reactor tubes for both catalysts was hypothesized to be due to catalyst precipitation, not due to coking.

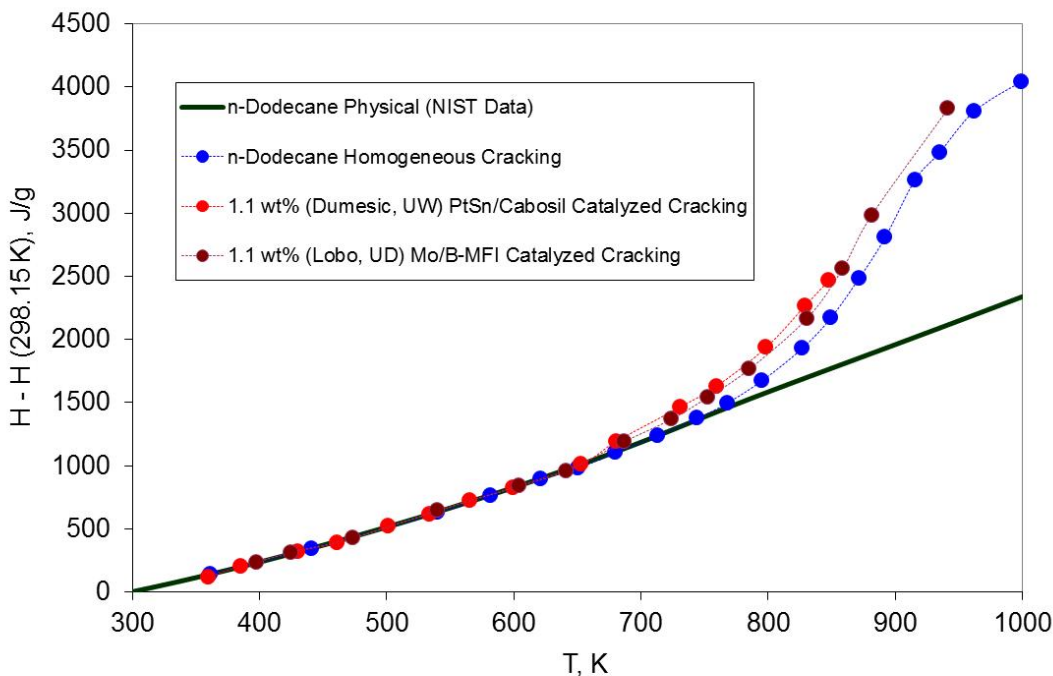


Fig. 20. Comparison of endotherms for *n*-dodecane conversion at 42 MPa with increasing temperature (*n*-dodecane has a critical temperature of 658 K and critical pressure of 1.8 MPa) with 1.1 wt% suspended catalysts, compared to neat *n*-dodecane pyrolysis and physical heat capacity.

4.0 Recommendations for Future Research

Develop advanced endothermic fuels based on jointly designed fuel molecule–catalyst systems:

- a) Optimize density and distribution of multi-functional catalyst sites, minimizing simultaneous interactions of fuel molecules with more than one site and undesirable bimolecular mechanisms.
- b) Design and synthesize catalyst supports for accommodating stable, yet reactive single-site Pt.
- c) Screen additional alkali and alkaline modifiers for balanced lattice electron delocalization and electron transfer to facilitate alkane dehydrogenation and alkene desorption.
- d) Identify approaches to titrate external framework or support sites to prevent outside-in coking and deactivation.

e) Design fuel-suspendable, combustible nanocatalysts that maximize available catalytic sites and minimize coke formation and deposition in heat exchanger channels.

5.0 References

- [1] MCCCSTowhee, <http://towhee.sourceforge.net>.
- [2] *a)* G. Kresse, and J. Hafner, “Ab initio molecular dynamics for liquid metals,” *Phys. Rev. B* 47 (1993) 558–561.; *b)* G. Kresse and J. Furthmuller, “Efficiency of ab-initio total energy calculations for metals and semiconductors using a plane-wave basis set,” *Comput. Mater. Sci.* 6 (1996) 15–50.
- [3] N. Rahimi and R. Karimzadeh, “Catalytic cracking of hydrocarbons over modified ZSM-5 zeolites to produce light olefins: A review,” *Appl. Catal. A: Gen.*, 398 (2011) 1–17.
- [4] X. Zhu, S. Liu, Y. Song, and L. Xu, “Catalytic cracking of C4 alkenes to propene and ethene: Influences of zeolites pore structures and Si/Al₂ ratios,” *Appl. Catal. A: Gen.*, 288 (2005) 134–142.
- [5] M. G. Suer, Z. Dardas, Yi. H. Ma, and W. R. Moser, “An in situ CIR–FTIR study of *n*-heptane cracking over a commercial Y-Type zeolite under subcritical and supercritical conditions,” *J. Catal.* 162 (1996) 320–6.
- [6] M.G. Martin and J.I. Siepmann, "Transferable potentials for phase equilibria. 1. United-atom description of n-alkanes," *J. Phys. Chem. B* 102 (1998) 2569–77.
- [7] *a)* P. E. Blöchl, “Projector augmented-wave method,” *Phys. Rev. B* 50 (1994) 17953–17979.; *b)* G. Kresse and D. Joubert, “From ultrasoft pseudopotentials to the projector augmented wave method,” *Phys. Rev. B* 59 (1999)1758–1775.; *c)* J. P. Perdew, K. Burke, and M. Ernzerhof, “Generalized gradient approximation made simple,” *Phys. Rev. Lett.* 77 (1996) 3865–3868.
- [8] S. J. Grimme, “Semiempirical GGA-type density functional constructed with a long-range dispersion Correction,” *Comp. Chem.* 27 (2006) 1787–1799.
- [9] S. M. Opalka and T. Zhu, “Influence of the Si/Al ratio and Al distribution on the H-ZSM-5 lattice and Brønsted acid site characteristics” *Micropor. Mesopor. Mater.*, 222 (2016) 256–270.

University of Delaware

Endothermic Cracking of Alkanes at High Pressures

PIs: Raul F Lobo and Dionisios G. Vlachos

Students and Postdocs: Edward Schreiner, Teketel Forsido (PD) and Huibo Shen

Part 1: Alkane Endothermic Cracking using Acid Zeolite Catalysts

The first part of our investigations focused on understanding the high-pressure cracking characteristics of acid zeolite catalysts. In particular, H-ZSM-5 catalysts are currently used (at low pressures) in the petrochemical industry for the cracking of mid-range distillate increasing the yield of olefins in the Fluidized Catalytic Cracking process. This observation motivated the investigation of these materials under high pressures. In parallel with these experimental investigations we attempted to understand the reaction mechanisms of *n*-pentane (and other small hydrocarbons) to develop a microkinetic model of this complex reaction process. The effects of temperature, pressure and weight hourly space velocity (WHSV) on the conversion of *n*-pentane on H-[Al]ZSM-5 were investigated to determine the potential of this reaction/catalyst system for endothermic cooling. *n*-Pentane was selected as the model reactant because it is the simplest liquid hydrocarbon at STP and has a high cooling potential (pentane cracking to ethane and propylene has a heat of reaction of 1.15 MJ/kg). In addition, *n*-pentane cannot form neutral aromatic species by cyclization and dehydrogenation without molecular weight growth,²⁸ potentially reducing the rate of coke-forming reactions. Coke formation was anticipated to be a potential problem for the long-term stability of these systems.

Figure 1 shows the conversion of *n*-pentane and product carbon selectivity at temperatures between 633 K and 723 K ($P = 40$ bar and WHSV of $1120 \text{ g}_{\text{C}_5}\text{g}_{\text{cat}}^{-1}\text{h}^{-1}$). Conversion increases rapidly with temperature and the major products of the reaction were propane and butane. At all experimental conditions investigated, the selectivity to methane,

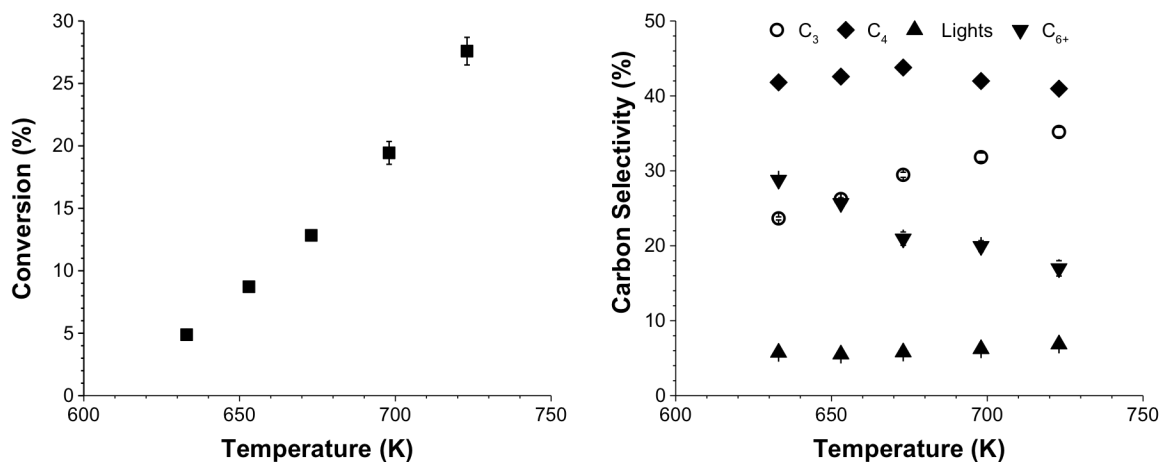


Figure 1: Conversion of *n*-pentane (left) and selectivity to product groups (right) during high pressure conversion on H-ZSM-5. Reaction conditions: $T = 633 - 723$ K, $P = 40$ bar, and $\text{WHSV} = 1120 \text{ g}_{\text{C}_5}\text{g}_{\text{cat}}^{-1}\text{h}^{-1}$

ethane, ethene, propene and butenes was low (<10%). As temperature increased, selectivity to propane increased, while selectivity to butane remained nearly constant. On the other hand, selectivity to higher molecular weight products (C₆₊) decreased with increasing temperature.

Increasing the pressure from 10 bar up to a total pressure of 30 bar, before the transition to the supercritical phase (34 bar), increases pentane conversion, but further increases in pressure up to 60 bar did not increase the total conversion. Pressure changes had little effect on the selectivity of the major products: propane and butane, but, increases in pressure decreased selectivity to the light products and increased selectivity to the heavier C₆₊ fraction.

We observed formation of more than 50 different species upon the reaction of *n*-pentane on H-[Al]ZSM-5 (Figure 2), including many compounds heavier than pentane; this is clear evidence of secondary bimolecular reactions in the catalyst controlling the product distribution at high pressure. In addition, the ratios of C₃/C₂ and C₄/C₁ products were greater than 1 under all conditions, which further indicates a role for bimolecular reactions in the catalyst pores. If monomolecular cracking reactions were dominant, the average H/C ratio of the cracked products would equal that of the feed (*n*-pentane H/C = 2.4), while the average H/C of products lighter than pentane was between 2.5 – 2.6. Since the observed C₁-C₅ species had an average H/C greater than the feed, either the olefins produced from monomolecular cracking were consumed in secondary reactions or paraffins were produced via a reaction other than *n*-pentane cracking.

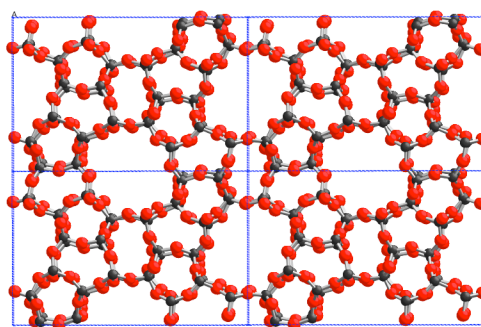


Figure 2. Framework structure of zeolite ZSM-5 (MFI) containing 10-ring (5.6 Å) pore apertures.

The consumption of olefins lighter than pentane through secondary bimolecular reactions is consistent with changes in the carbon selectivity of the light olefins ethene, propene, and butene. Carbon selectivity of the light olefins decreased with increasing pressure, with the change being most clear at pressures below ~ 30 bar, where pentane is gas-like. Elevated pressures promote oligomerization of olefins, a reaction also observed here. Carbon selectivity of the light olefins also increased with increasing WHSV, that is, with less time to react, a greater percentage of light olefins formed through monomolecular and bimolecular cracking of pentane survived without undergoing further reactions. From the observed trends in carbon selectivity of the light olefins, a simplified reaction network can be created to illustrate the formation of the major products: propane and butane (Figure 3).

If monomolecular cracking were the dominant reaction channel, as pressure increases, the apparent activation energy should also increase and approach the intrinsic activation energy. This trend occurs because saturation is reached at elevated pressures, reducing the effect of adsorption enthalpy on the apparent activation energy. In contrast, it was observed

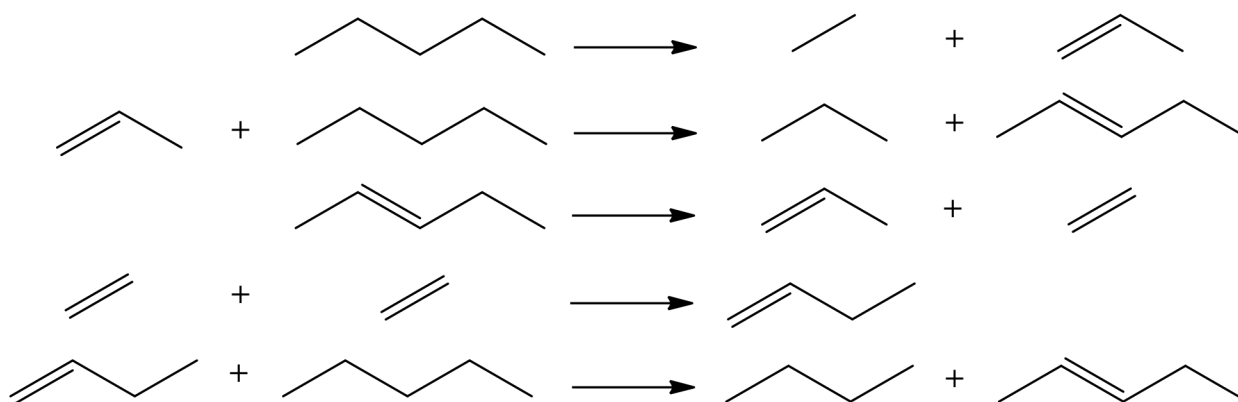


Figure 3: Simplified reaction network illustrating a possible path to the production of propane and butane via cracking and hydride transfer reactions

that the apparent activation energy based on consumption of *n*-pentane decreases with increasing pressure, which is opposite of the expected trend for monomolecular cracking. Furthermore, at 40 bar, the apparent activation energy for the consumption of *n*-pentane was 86 kJ/mol, which was much less than expected for monomolecular cracking, but consistent with the results obtained using other zeolite frameworks as solid acid catalysts.

The high selectivity (>70%) to propane and butane, along with the observed changes in the selectivity to other lights and C₆₊ compounds, indicate that bimolecular reactions, such as hydride transfer and alkylation, control product distribution. While the product distribution from the high-pressure conversion of pentane resulted in an endothermic process, hydride transfer reactions led to the transformation of high energy olefins into lower energy paraffins and aromatics, resulting in a decrease of the process endothermicity. Hydride transfer occurs readily on H-ZSM-5 and other acid zeolites, and an alternative catalyst that suppresses these reactions should improve selectivity to light olefins, which will increase cooling capacity of the endothermic fuel. We think that to avoid high-molecular weight products and the hydrogen redistribution processes observed here, catalysts that have essentially no acid sites are needed.

Part 2: Non-Acidic Zeolite-Supported Molybdenum Carbide Catalysts

We have found that molybdenum carbides, supported on carbon and alumina, lead to high selectivity to the formation of pentenes. Further investigation of molybdenum carbides on different supports and reaction conditions lead to the discovery of a novel Mo-containing non-acidic zeolite that displays exceptional properties for alkane activation.

Mo-supported zeolite catalysts have been known for more than a decade. They are used primarily for the activation of methane into benzene and hydrogen at high temperatures, but this reaction depends not only on the ability of MoC_x nanoparticles to activate methane, but

also on the ability of the zeolite acid sites to oligomerize and dehydrogenate the product. **We have discovered a new catalytic material** that retains the high activity for C-H bond activation of the nanostructured MoC_x particles while eliminating the acid sites. This has been achieved by incorporating the MoO_3 precursor into boron-containing ZSM-5 and in siliceous zeolites containing no trivalent framework elements, but containing internal defects (silanol groups) that can react and anchor the MoO_3 precursor.

Catalyst Synthesis and Characterization

Low acidity zeolites were prepared using tetrapropylammonium as structure director and using boric acid as the source of heteroatoms. Depending on the conditions, Si/B ratios of 15-80 can be achieved. All the zeolites investigated have the MFI-type framework structure.

We also prepared siliceous zeolites containing no aluminum and no boron to assess the effect of the framework change on the activity of the molybdenum carbide particles.

To incorporate the Mo into the zeolite, the desired mass of ammonium heptamolybdate ($(\text{NH}_4)_6\text{Mo}_7\text{O}_{24}$) was weighed out to yield a 5.8% metal loading of Mo/support. The samples were prepared by impregnation with ammonium heptamolybdate. The dry samples are then calcined in air. Prior to reaction the catalyst is carburized in methane (20%, H_2 balance) at 650°C for 4 h. The composition of the sample was optimized to maximize the conversion of n-pentane at relevant temperature and operating pressures (30-60 bar).

We investigated a number of pure and supported molybdenum carbides for the conversion of pentane at 40 bar of total pressure. Figure 4 compares the reaction rates of pentane conversion over several Mo-carbide catalysts. Two samples show the highest reactivity: $\text{Mo}_x\text{C}/[\text{B}]\text{ZSM-5}$ (zeolite support) and $\text{Mo}_x\text{C}/\gamma\text{-Al}_2\text{O}_3$. Also of note is that in these two catalysts the maximum activity is not observed at zero time on stream, but it is observed as a peak about 1 hr after starting the reaction. This indicates that the active catalyst phase is formed *in the reactor* by interaction with the reactant phase. For both the alumina and the zeolite supports there is a slow deactivation rate that is not stabilized after 5 hr of time on stream. In addition to the conversion of the pentane, we investigated the selectivity of the catalysts and in both cases ($[\text{B}]\text{ZSM-5}$ and $\gamma\text{-Al}_2\text{O}_3$) the selectivity towards pentenes (mostly 2-pentene) is between 85% and 90% for the 5 hr of catalyst testing. The other catalysts investigated are less reactive and much less selective forming a variety of smaller products (cracking reactions). Because of their high reactivity, most of the following investigations were performed on the $[\text{B}]\text{ZSM-5}$ and alumina supported catalysts.

The effect of the amount of Mo loaded in the samples on the catalytic activity was optimized. We observed steady increases in reactivity up to a concentration of approximately 4% w/w of

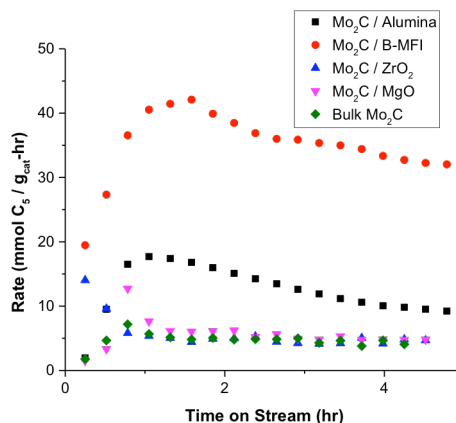


Figure 4: Rates of conversion of pentane over various Mo carbide catalysts. Conditions: 40 bar, 0.5 mL/min of pentane, 723 K, $m_{\text{cat}} = 100$ mg, $\text{WHSV} = 188$ $\text{gC}_5/\text{g}_{\text{cat}}$ hr, residence time ~ 0.6 s.

Mo/[B]ZSM-5 with very little difference in the selectivity of the catalysts. Consequently we have fixed the composition of the Mo/[B]ZSM-5 samples to contain 5.8% w/w of Mo.

We have also investigated the effect of B on the catalyst performance by preparing Mo-containing MFI catalysts with no B or Al. These siliceous samples were prepared with a high- and low-concentration of internal defect sites to assess as well, the role of defect sites on the formation and activity of the catalysts. We have found that the B-containing catalysts are 3-4 times more active than the samples prepared on siliceous zeolites. It is clear that B plays an important role in the formation of the active Mo-carbide phase. Understanding how is the B improving the reactivity is one of the objectives of the upcoming funding period.

Under the reaction conditions investigated the presence of Mo increases the pentane conversion many times, especially at low temperatures. The activation energy over the catalyst is one half than the activation energy over the support (102 kJ/mol vs. 201 kJ/mol) but because the gas phase reaction activation energy is higher, there is a temperature at which the homogeneous chemistry is going to dominate over the catalytic chemistry. This temperature can be estimated by extrapolation from the graph to be $\sim 550^{\circ}\text{C}$, and shows that below this temperature catalytic chemistry will dominate the conversion and selectivity of the reactor, while at higher temperatures the gas phase chemistry will dictate both conversion and selectivity for the system.

We also investigated other factors on the properties of the catalysts. Using pentane as the reactant, the total pressure was changed from 20-60 bar finding that the over all conversion, selectivity and reaction rates are weakly affected by pressure. This observation means that under these reaction conditions the catalyst surface is saturated with hydrocarbons and that further increases in the pressure of the reactant will not increase neither the conversion or drastically change the selectivity of the catalysts.

The catalysts were reactivated by oxidizing in air at 550°C and were subsequently re-carburized in methane/H₂ mixtures. Catalytic tests of the reactivated catalysts reveal that there is in fact a small improvement in the reactivity of the samples (higher conversions and reaction rates) upon reactivation. Little changes in the pattern of selectivity were observed as well suggesting that the catalyst sites of the Mo-carbide nanoparticles can be reformed without loss through this oxidation/carburization reactivation step.

We compared the reactivity of the Mo/[B]ZSM-5 and Mo/Al₂O₃ catalyst using pentane and heptane finding important differences in the observed conversion and selectivity patterns. First, conversion of pentane is higher than the conversion of heptane in both catalysts; this is unexpected since the critical pressure of pentane is higher than the critical pressure for heptane and thus a higher concentration of the heavier hydrocarbon in the catalysts pores is expected. There are important differences in the selectivity pattern indicating that hydrocarbons higher than C₅ (and C₆) can react through a different reaction mechanism than dehydrogenation. Table 1 summarizes the carbon selectivity to the various products. For pentane the dominant product is pentenes for both the [B]ZSM-5 and Al₂O₃ supported catalysts with small amounts of smaller hydrocarbons present in the product stream (mostly butenes and propene). In the case of the reactivity of heptane over Mo/[B]ZSM-5, the

dehydrogenation product (C7=, heptenes) is a small fraction of the product stream. The most important products are C6/C6= (21%), C4/C4= (30%) and C3/C3= (25%). In fact the alkenes are present at higher concentrations than the alkanes, a highly desired because these products are the result of highly endothermic reactions.

Table 1: Comparison of the selectivity of pentane and heptane conversion over Mo-carbide catalysts supported on alumina and MoC_x@[B]ZSM-5.

		Average Carbon Selectivity, %										
		C1	C2	C2=	C3	C3=	C4	C4=	C5	C5=	C6	C7=
MoC _x @/[B]ZSM-5	C5	0.72	1.92	0.25	1.57	2.29	0.76	5.14		86.5	0.8	
	C7	0.96	4.4	1.53	8.54	15.1	9.9	20.1	1.5	7.8	21	8.83
Mo/Al ₂ O ₃	C5	1.76	5.4	1.18	1.75	7.24	0.04	6.01		76.5	0	
	C7	0.58	3.3	1.05	5.08	5.75	6.51	7.03	1.4	5.1	19.8	45.1

P = 40 bar, T = 723 K and WHSV = 188 g/g_{cat} hr

Perhaps the most important property of the MoC_x@[B]ZSM-5 catalyst investigated here is that they are able to break C-C bonds at rates that are somewhat lower than the rates observed over acid zeolites, but that have little if any ability to carry out hydride transfer reactions shifting hydrogen from high-to-low molecular weights and decreasing the endothermicity of overall process. The impact on selectivity is best observed by comparing the reactions observed over the MoC_x@[B]ZSM-5 on n-heptane (Figure 5).

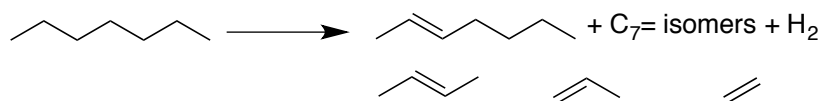


Figure 5. MoC_x@[B]ZSM-5 catalyst produce dehydrogenation and cracking products but form very few higher molecular weight products. There is essentially no sign of Brønsted catalysis in these systems and there is only a very small fraction of aromatic products (toluene) formed.

Most recently, the research has focused on the analysis of $\text{Mo}_x\text{C}@[B]\text{ZSM-5}$ catalysts using a variety of techniques. In particular, TEM investigations of the catalysts showed that the most active materials have in fact a distribution of carbide nanoparticles, with many particles inside the zeolite nanopores, but also with many particles present in the external surface of the zeolite. The exterior particles are much larger than the interior particles and make characterization of the samples difficult. To minimize the effect of this distribution of carbide particles in and outside the zeolite, we reduced the molybdenum content (to 2%) until no further particles were observed outside the zeolite pores. TEM images of these model $\text{Mo}_x\text{C}@[B]\text{ZSM-5}$ materials show that the carbide particles in the zeolite pores are very uniform and of about 3 nm in diameter (Figure 6).

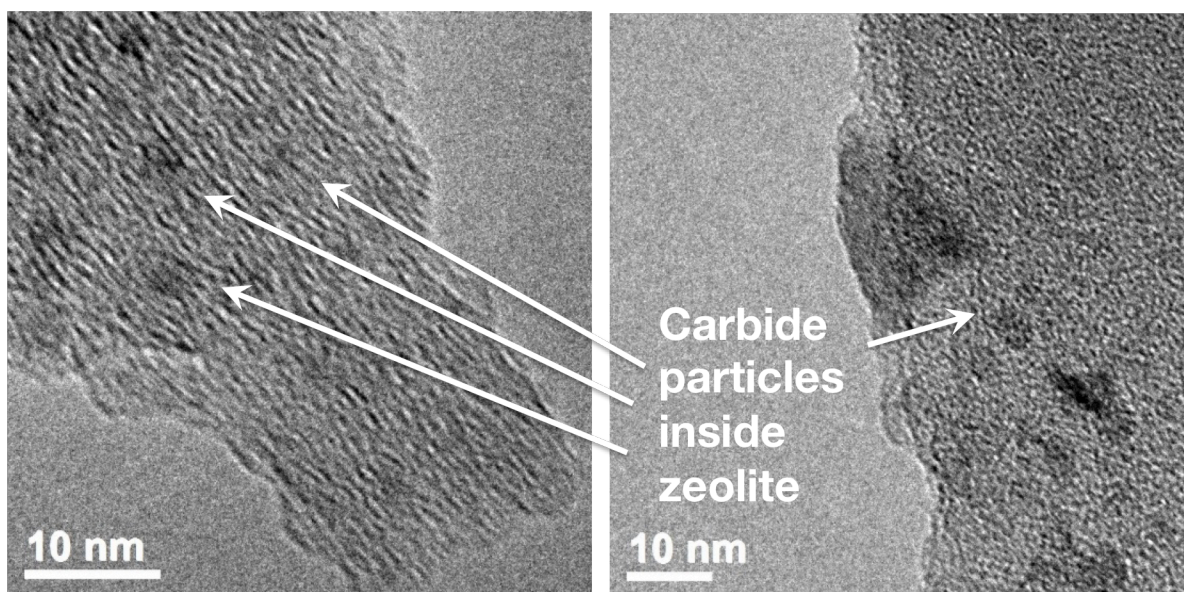


Figure 6. TEM image of a $\text{Mo}_x\text{C}@[B]\text{ZSM-5}$ sample containing ~2% Mo composition. Note the observation of particles inside the zeolite pores.

The samples were also investigated using X-ray absorption spectroscopy. The experiments followed the oxidation state of the molybdenum as a function of sample treatment. The experiments showed that upon calcination of the heptamolybdate-containing sample, the dispersion of the molybdenum increased. This is consistent with a model in which the MoO_3 can desorb, go to the gas phase and anchor inside the zeolite pores. The samples were then reduced in hydrogen showing the formation of small metal-like nanoparticle inside the zeolite pores. The carburization of the sample showed the formation of a carbide-like Mo species, but the XANES spectrum is not fully consistent with the spectrum of Mo_2C , that is the zeolite samples contain disordered forms of Mo_2C , or some large number of very small dimers or trimers that are detected by spectroscopy but are not detected using classical TEM techniques.

Part 3: Future Directions

Through this program we have investigated two classes of materials for catalyzing endothermic alkane reactions at high temperatures and pressures. The first group of catalysts,

acid zeolites, showed high reaction rates, reasonable stability (hours) but not good selectivity to the most desired products, small alkenes formed by cracking of larger alkanes. The second group of catalysts, based on supported molybdenum carbides, showed high selectivity to alkenes, but relatively little selectivity to breaking C-C bond and forming smaller hydrocarbons. In addition, the reaction rates on the $\text{MoC}_x\text{@[B]ZSM-5}$ materials are lower than on the acid zeolites (about 3-5% of the overall conversion at similar conditions).

In the future we wish to investigate materials that may have the desirable properties of these two classes of materials. Because of their high activity and stability, zeolites remain high in the list of potential targets but they should be such that they have little acidity if any. One candidate is zinc-exchanged zeolites. Zn-[Al]ZSM-5 type materials have been used for propane aromatization where the Zn^{2+} cations help with the dehydrogenation of the alkanes, and the acid portion of the zeolite catalyzes C-C bond formation and hydride transfer. We suggest that this class of materials, where the framework Al atoms are substituted with B—to reduce the acidic properties of the material—or where there is a high level of Zn exchange such that the number of acid sites is small, could potentially yield the desired combination of dehydrogenation reactions and C-C bond scission that is desired to achieve high endothermicity of hydrocarbon conversions.

AFOSR Deliverables Submission Survey

Response ID:6651 Data

1.

1. Report Type

Final Report

Primary Contact E-mail

Contact email if there is a problem with the report.

amdean@mines.edu

Primary Contact Phone Number

Contact phone number if there is a problem with the report

303-273-3643

Organization / Institution name

Colorado School of Mines

Grant/Contract Title

The full title of the funded effort.

Heterogeneously Catalyzed Endothermic Fuel Cracking

Grant/Contract Number

AFOSR assigned control number. It must begin with "FA9550" or "F49620" or "FA2386".

FA9550-12-1-0495

Principal Investigator Name

The full name of the principal investigator on the grant or contract.

Anthony M.Dean

Program Manager

The AFOSR Program Manager currently assigned to the award

Michael Berman

Reporting Period Start Date

09/30/2012

Reporting Period End Date

05/31/2016

Abstract

The objective of this project was to develop and apply fundamentally based experimental and computational methodologies that can lead to the design of improved supercritical fuel/catalyst/heat exchanger systems for cooling hypersonic vehicles. This project was a multi-team effort involving researchers at the University of Delaware, United Technologies Research Center, and the Colorado School of Mines.

Advances in catalytic studies include:

- Developed and applied modeling and software tools to high-pressure chemically reacting processes, including supercritical behavior.
- Developed models to evaluate the influence of low levels of steam addition for reducing the production of polyaromatics and mitigating catalyst-fouling carbon deposits.
- Developed new microstructural models to represent catalytic performance in washcoated monolith structures.
- Measured impact of Pt-exchanged H-ZSM-5 on heptane conversion and selectivity.

DISTRIBUTION A: Distribution approved for public release.

- Measured impact of cesium ion exchange for protons in Pt/H-ZSM-5 catalysts.
- Carried out high-pressure kinetic studies of hydrocarbon cracking reactions over MoCx nanoparticles supported on non-Acidic Zeolites, specifically [B]ZSM-5 zeolites.
- Conducted fundamental investigations of the catalysts using kinetic studies of methane activation, X-ray absorption spectroscopy and transmission electron microscopy.
- Designed aluminosilicate zeolite-based catalyst model systems using combined experimental–theoretical methodologies.
- Performed specially tailored real-time spectroscopic catalytic reactor studies with n-pentane and n-heptane.
- Applied density functional calculations to characterize catalyst model systems with varying Si/Al ratios.

Advances in high-pressure gas phase pyrolysis include:

- Measured ethane, pentane and hexane pyrolysis over range of pressures, temperatures and residence times
- Comparisons of conversion, major product distributions and molecular weight growth processes to detailed kinetic mechanisms demonstrate that mechanism can properly account for wide variations in pressure, including supercritical pressures.

Successfully tested candidate catalysts under supercritical fuel conditions in UTRC Heat Exchanger rig.

Distribution Statement

This is block 12 on the SF298 form.

Distribution A - Approved for Public Release

Explanation for Distribution Statement

If this is not approved for public release, please provide a short explanation. E.g., contains proprietary information.

SF298 Form

Please attach your SF298 form. A blank SF298 can be found [here](#). Please do not password protect or secure the PDF

The maximum file size for an SF298 is 50MB.

[AFD-070820-035.pdf](#)

Upload the Report Document. File must be a PDF. Please do not password protect or secure the PDF . The maximum file size for the Report Document is 50MB.

[2016 final report.pdf](#)

Upload a Report Document, if any. The maximum file size for the Report Document is 50MB.

Archival Publications (published) during reporting period:

T. Zhu, S. M. Opalka, Z. Dardas, and S. C. Emerson, "Cylindrical Internal Reflectance-Fourier Transform Infrared Reactor Studies of Supercritical Pentane Cracking over Zeolite Catalysts," submitted to Appl. Catal. A: Gen.

S. M. Opalka and T. Zhu, "Influence of the Si/Al ratio and Al distribution on the H-ZSM-5 lattice and Brønsted acid site characteristics" Micropor. Mesopor. Mater., 222 (2016) 256-270.

S. M. Opalka, H. Huang, and X. Tang, "Mechanistic investigations of heterogeneously catalyzed steam gasification of coke precursors," Energy & Fuels, 28(10) (2014) 6188-6199.

Canan Karakaya, Robert J. Kee, "Progress in the direct catalytic conversion of methane to fuels and chemicals" Progress in Energy and Combustion Science, 55 (2016) 60–97.

Robert J. Kee, Canan Karakaya, Huayang Zhu, "Process intensification in the catalytic conversion of natural gas to fuels and chemicals" Proceeding of the Combustion Institute (2016) 1–26 (in press).

Canan Karakaya, Huayang Zhu, Robert J.Kee, "Kinetic modeling of methane dehydroaromatization chemistry on Mo/Zeolite catalysts in packed-bed reactors" Chemical Engineering Science 123 (2015) 474–486.

C. Karakaya, P.J. Weddle, J.M. Blasi, D.R. Diercks, and R.J. Kee, "Modeling reaction-diffusion processes within catalyst washcoats: I. Microscale processes based on three-dimensional reconstructions," Chem. Eng. Sci., 145:299-307, (2016).

J.M. Blasi, P.J. Weddle, C. Karakaya, D.R. Diercks, R.J. Kee, "Modeling reaction-diffusion processes within catalyst washcoats: II. Macroscale processes informed by microscale simulations," Chem. Eng. Sci., 145:308-316, (2016).

Canan Karakaya, Selene Hernandez Morejudo, Huayang Zhu, Robert J. Kee, "Catalytic chemistry for methane dehydroaromatization (MDA) on a bifunctional Mo/HZSM-5 catalyst in a packed bed" Ind. Eng. Chem. Res. (submitted).

Saldana, M. H.; Bogin Jr, G. E., "Investigation of n-pentane pyrolysis at elevated temperatures and pressures in a variable pressure flow reactor" Journal of Analytical and Applied Pyrolysis 118, (2016), 286-297.

Mario H. Saldana, Gregory E. Bogin, Kun Wang, and Anthony M. Dean, "Comparative Kinetic Analysis of Ethane Pyrolysis over an Extended Pressure Range" Energy Fuel (submitted).

2. New discoveries, inventions, or patent disclosures:

Do you have any discoveries, inventions, or patent disclosures to report for this period?

No

Please describe and include any notable dates

Do you plan to pursue a claim for personal or organizational intellectual property?

Changes in research objectives (if any):

none

Change in AFOSR Program Manager, if any:

none

Extensions granted or milestones slipped, if any:

6 month no-cost extension granted

AFOSR LRIR Number

LRIR Title

Reporting Period

Laboratory Task Manager

Program Officer

Research Objectives

Technical Summary

Funding Summary by Cost Category (by FY, \$K)

	Starting FY	FY+1	FY+2
Salary			
Equipment/Facilities			
Supplies			
Total			

Report Document

Report Document - Text Analysis

Report Document - Text Analysis

Appendix Documents

2. Thank You

E-mail user

Aug 10, 2016 15:22:47 Success: Email Sent to: amdean@mines.edu